



JGR Atmospheres

RESEARCH ARTICLE

10.1029/2024JD043270

Key Points:

- Rain cells further ahead of a front exhibit a wide range of raindrop sizes but with a low concentration of raindrops
- The high-altitude westerly winds accompanying a front can influence areas up to 300 km ahead of it
- Rain cells ahead of the front within 200–300 km exhibit precipitation microphysics most similar to warmsector rainfall

Supporting Information:

Supporting Information may be found in the online version of this article.

Correspondence to:

Y. Chen, chenylun3@mail.sysu.edu.cn

Citation:

Zuo, H., Chen, Y., Liu, T., Zhang, A., Chen, S., & Li, W. (2025). Frontal structure effects on precipitation microphysics in South China rain cells. *Journal of Geophysical Research: Atmospheres*, *130*, e2024JD043270. https://doi.org/10.1029/2024JD043270

Received 25 DEC 2024 Accepted 14 OCT 2025

Frontal Structure Effects on Precipitation Microphysics in South China Rain Cells

Haosheng Zuo^{1,2} , Yilun Chen^{1,2} , Tianao Liu^{1,2} , Aoqi Zhang^{1,2} , Shumin Chen^{1,2}, and Weibiao Li^{1,2}

¹School of Atmospheric Sciences and Key Laboratory of Tropical Atmosphere-Ocean System, Ministry of Education, Sun Yat-sen University, Zhuhai, China, ²Southern Marine Science and Engineering Guangdong Laboratory (Zhuhai), Zhuhai, China

Abstract Frontal and warm-sector rainfall are typical precipitation types in South China during the presummer rainy season. However, current classification methods mostly rely on subjective judgment. The precipitation microphysical traits of rain cells in South China during the pre-summer rainy season were investigated using 8 years of observations from a spaceborne precipitation radar. We segment regions every 100 km ahead of the front, resulting in four areas (0–100, 100–200, 200–300, and >300 km). Convection thrives in rain cells located 0–100 and 200–300 km ahead of the front, but is suppressed in the other two areas. Rain cells in the 0–100 km area exhibit dominant ice-phase processes, with the highest raindrop concentration and smallest raindrops. However, rain cells in the 200–300 km area are characterized by the coexistence of liquid-and ice-phase processes, yielding the largest raindrops. These findings provide valuable insights into the precipitation microphysics ahead fronts in South China in the pre-summer rainy season.

Plain Language Summary Precipitation types can be mainly divided into frontal rainfall (FR) and warm-sector rainfall (WR) in South China. In the current context of global warming, these two types of precipitation may be becoming more frequent, causing floods and severe disasters. However, we do not know exactly where the boundary between FR and WR lies. Here, we used 8 years of high-resolution satellite observations of a typical monsoonal coastal region (South China) to analyze how the vertical structure of precipitation in rain cells situated on the warm side of a front changes with increasing distance ahead of the front. The results show that heavy rainfall in the warm areas is more likely to occur in the 200–300 km area ahead of the front, rather than at other distances.

1. Introduction

The pre-summer rainy season in South China generally lasts from April to the end of June (Luo et al., 2020). Rainfall during this period often leads to floods and severe disasters, exerting a significant impact on both society and the environment (Chen et al., 2019; Luo et al., 2017). Because of global warming, such extreme precipitation and related disasters are becoming more frequent (Kundzewicz & Pińskwar, 2022; Li et al., 2022; Song et al., 2022). The main precipitation types in South China are frontal rainfall (FR) and warm-sector rainfall (WR) (Song et al., 2022; Wu & Luo, 2016). Previous studies have shown that FR is closely related to the strong forcing of synoptic-scale systems (Tao, 1987), whereas WR occurs in weak synoptic forcing or far ahead of the front (Huang et al., 1986). WR generally refers to heavy rainfall occurring on the warm side of a front, typically 200– 300 km ahead of the surface front, or within the convergence zone between southwesterly and southeasterly winds (Huang et al., 1986; Luo et al., 2017). It usually develops in a southwesterly moist flow without significant lowlevel directional shear (i.e., no intrusion of northerly winds, and vertical wind shear <5 m/s), and is not associated with tropical systems, defined here as the absence of tropical depressions or stronger cyclones (maximum sustained winds ≥17.2 m/s) over the South China Sea during the event, and sea surface temperature <26°C (Huang et al., 1986; Wu et al., 2020). The forcing factors for WR are highly complex, including offshore regional convergence caused by low-level jets (Wu & Luo, 2016; Zhong & Yang, 2020), uneven underlying surface forcing (Chen et al., 2014; Rao et al., 2022), and the triggering of a convectively generated cold pool (Liu et al., 2018; Wu & Luo, 2016). Both types of precipitation have been well-documented from dynamic and thermodynamic perspectives in previous studies. However, the focus has mainly been on the large-scale environmental fields during heavy precipitation, with a relative lack of attention paid to the local environmental field

© 2025. American Geophysical Union. All Rights Reserved.

ZUO ET AL. 1 of 23

information based on the perspective of each rain cell. This gap hampers our understanding of precipitation microphysical processes.

During the pre-summer rainy season in South China, FR and WR can appear in isolation (Li & Du, 2021; Wang et al., 2021; Wu et al., 2020), or simultaneously (Han et al., 2021; Li & Du, 2021). Therefore, the classification of FR and WR is vital but difficult. The first difficulty is the identification and positioning of the front (Li & Du, 2021). The terrain in South China is mountainous, resulting in unobvious frontal characteristics of the surface wind field (Wu et al., 2020). The second difficulty is that there are some precipitation events that show a combination of FR and WR microphysical characteristics (Han et al., 2021), the existence of which means that forcibly dividing or subjectively discarding rain cells will result in a loss of information. For example, if the precipitation is categorized artificially based on the distribution of sea or land and the distance ahead of the front, inland precipitation occurring ahead of the front within 200 km would be FR, whereas coastal precipitation occurring more than 200 km ahead of the front would be WR (Han et al., 2021; Wu et al., 2020). However, inland precipitation more than 200 km ahead of the front and coastal precipitation within 200 km are usually discarded due to displaying atypical precipitation characteristics. WR and FR types can also be differentiated according to their occurrence in weak or strong synoptic-scale environments (Li & Du, 2021). However, such an approach may lead to overestimation of FR intensity, classifying isolated convection far from the front as WR, and even confusing precipitation types in the areas within 100–200 km and >300 km ahead of the front. Moreover, existing classifications are mainly performed subjectively (Han et al., 2021; Wu et al., 2020), and tend to prioritize heavy rainfall over weak rainfall (Li & Du, 2021; Wu et al., 2020; Zhao et al., 2007). This limits our ability to gain an accurate understanding of the different types of precipitation during the pre-summer rainy season.

In order to accurately understand the microphysical processes of precipitation, many previous studies have analyzed the microphysical properties of convective precipitation based on ground-based raindrop disdrometers and dual-polarization radar (Huo et al., 2019; Luo et al., 2020; Yu et al., 2022). Some studies have compared the mean mass-weighted drop diameter (D_m) and the drop concentration parameter (N_w) of precipitation at heights below 5 km (Han et al., 2021; Yu et al., 2022). They found that WR had stronger convection intensity and larger raindrop sizes compared to FR. Although the variables observed by these ground-based instruments can be used as proxies for the intensity of convection and low-level microphysical processes in the liquid phase, in extreme precipitation events, factors such as the large raindrop effective radius and the high raindrop concentrations lead to large path-integrated attenuations, which may cause large losses of information on upper-level precipitation (Delrieu et al., 2000; Uijlenhoet & Berne, 2008). The Global Precipitation Measurement satellite dual-frequency precipitation radar provides a new perspective for precipitation microphysics research (Iguchi et al., 2012; Zhang, Chen, et al., 2023). These spaceborne precipitation radars excel at capturing high-altitude precipitation signals, experiencing less interference from the underlying surface. They also offer more consistent detection results across different times and locations (Fu et al., 2018). The application of GPM DPR can compensate for the shortcomings of ground-based instruments in accurately describing the ice-phase precipitation properties. Previous studies have conducted a statistical comparison between the precipitation microphysical characteristics of 80 oceanic storm events captured by GPM and ground-based radar observations, finding that the detection results of both were largely consistent (Chandrasekar & Le, 2015). During the Meiyu season, comparisons with groundbased observations indicated that the D_m and N_w retrieved from GPM DPR data showed good agreement with ground-based measurements (Sun et al., 2020). Additionally, a comparative study with S-band polarimetric radar in South China found that D_m exhibited good consistency with ground-based observations, whereas N_w was underestimated (Huang et al., 2021). These studies demonstrate the reliability of GPM DPR data, though some limitations remain in certain aspects.

In this study, we employed 8 years of spaceborne dual-frequency precipitation radar data to investigate the precipitation microphysical traits of rain cells in South China during the pre-summer rainy season. The use of spaceborne radar offers complementary perspectives on upper-level microphysical processes in extreme precipitation. Primarily, we objectively compared the vertical structure of rain cells at different distances ahead of the front, including weak precipitation. In addition, the local environmental field information was examined from the rain cell perspective. Furthermore, we investigated the range of distances ahead of the front at which WR is most likely to develop and the possible reasons for this based on the classification approach in this study. Ultimately, the aim was to provide a scientific basis for the separation of FR and WR.

ZUO ET AL. 2 of 23

com/doi/10.1029/2024JD043270 by Yilun Chen - Zhongshan University

Wiley Online Library on [27/10/2025].

Figure 1. Data processing flow chart, including data preprocessing, identification, and matching of rain cells and fronts.

This paper focuses on rain cells in South China during the pre-summer rainy season, whose microphysical characteristics are obviously related to the distance from the front. The data and methods employed in the study are briefly described in Section 2, followed by a comparison of the differences in microphysical characteristics and mechanistic explanations of rain cells in the four areas in Section 3. The vertical distribution of phase states and the relationship with precipitation intensity are discussed in Section 4. Finally, a summary is provided in Section 5.

2. Data and Methods

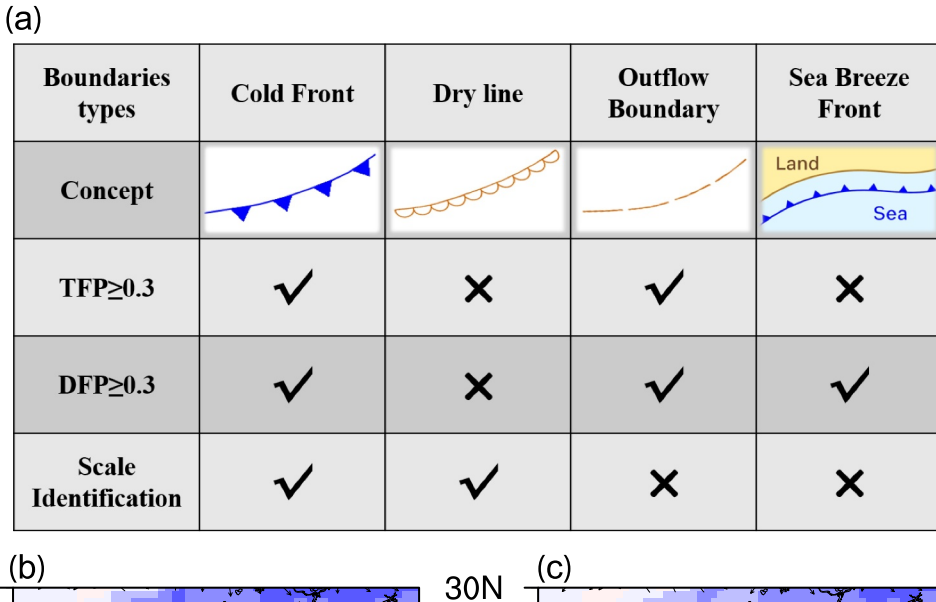
Data processing mainly involved GPM-2ADPR and ERA5. Initially, data within the specified longitudinal and latitudinal range of the study area were selected, followed by rain cell identification using the connected domain identification algorithm. Rain cells consisting of fewer than four grids were excluded. Fronts were then identified based on thresholds of dynamic and thermal parameters. Subsequently, rain cells and fronts were matched, classified, and subjected to feature extraction (Figure 1). The process is described in detail below.

2.1. Data

We used GPM-2ADPR version 7 precipitation data from April to June for a total of eight years from 2015 to 2022 provided by the Global Precipitation Measurement Mission website (https://gpm1.gesdisc.eosdis.nasa.gov). 2ADPR provides single- and dual-frequency-derived precipitation estimates from the Ku and Ka radars of the DPR on the GPM Core Observatory (Iguchi & Meneghini, 2021), with a spatial resolution of 5 km (Huffman et al., 2020). Version 7 is the first standard product to incorporate the Ka-band Precipitation Radar (KaPR) scan pattern changes implemented on 21 May 2018 (Huffman et al., 2020). This change in scan pattern provides a more accurate precipitation estimation method for dual frequency radar, Ku-band and Ka-band Precipitation Radar (KuPR and KaPR), to be applied to the entire observation swath (Seto et al., 2021). These data provide vertical profiles of drop size distribution (DSD) and radar reflectivity. Drop size distribution (DSD) consists of the normalized drop concentration parameter (dBN_w) and the mean mass-weighted drop diameter (D_m). The units of

ZUO ET AL. 3 of 23

21698996, 2025, 20, Downloaded from https://agupubs.onlinelibrary.wiley.com/doi/10.1029/2024JD043270 by Yilm Chen - Zhongshan University , Wiley Online Library on [27/10/2025]. See the Terms



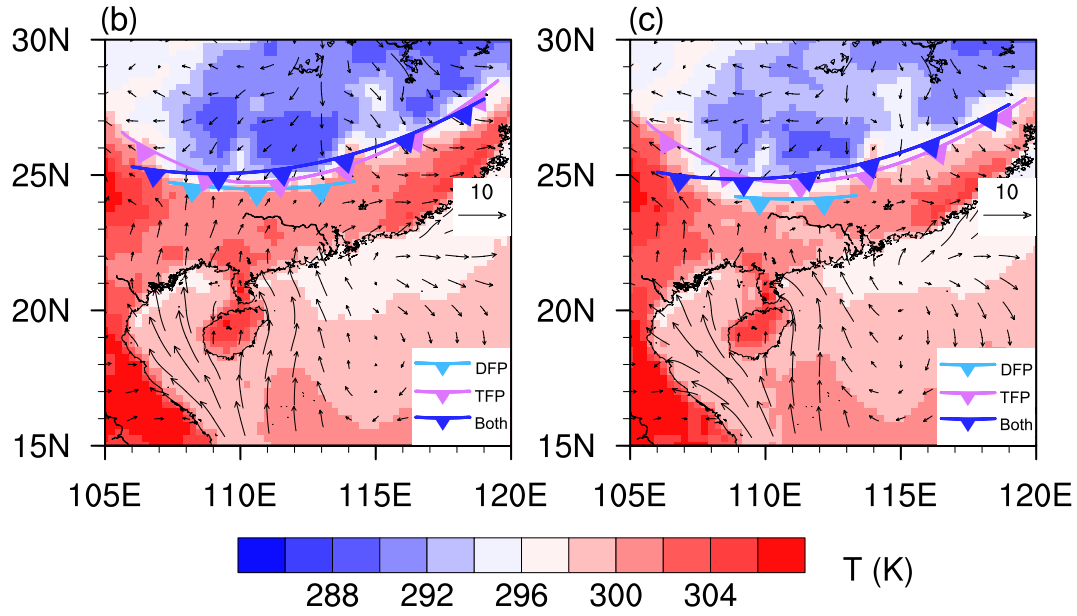


Figure 2. Panel (a) is a conceptual diagram illustrating the responses of the Thermodynamic Front Parameter (TFP) and Dynamic Front Parameter (DFP) to idealized frontal and non-frontal structures, highlighting their ability to distinguish cold fronts or convective-scale features. Panels (b) and (c) are schematic representations of the front identification results, showing the near-surface wind field and temperature distribution at 06:00 and 09:00 UTC on 19 April 2020, respectively. Light blue, purple, and dark blue lines represent the frontal positions determined using only DFP, only TFP, and the combination of both parameters, respectively.

 N_w and D_m are mm⁻¹m⁻³ and mm, respectively. Drop size distribution has been shown to be in good agreement with ground-based observations in limited local areas around the world (Petracca et al., 2018; Ryu et al., 2021). The minimum detectable radar reflectivity factor is 15.46 dBZ for KuPR and 19.18 dBZ for KaPR (Masaki et al., 2020). In addition, we used NASA's Integrated Multi-satellitE Retrievals for GPM data to provide precipitation data for the conceptual model (Jin et al., 2021).

The study region in South China covered $20^{\circ}-30^{\circ}N$, $105^{\circ}-120^{\circ}E$ (Figures 2b and 2c), and the study focused only on precipitation over land. In addition, the temperature, wind speed and direction, specific humidity, geopotential height and other environmental variables used in this study for front identification and mechanistic explanation were provided by ERA5—the latest generation of reanalysis data provided by the European Centre for Medium-Range Weather Forecasts (Hersbach et al., 2023). The resolution of these data is $0.25^{\circ} \times 0.25^{\circ}$, with 37 vertical

ZUO ET AL. 4 of 23

levels and a time interval of 1 hr, which is well suited to the needs of FR and WR research. Some variables in ERA5 are not assimilated from observations but are parameterized, which can sometimes lead to results that are inconsistent with observations (Lavers et al., 2022). ERA5 is influenced by parameterization, leading to an overestimation of Convective available potential energy (CAPE) and an underestimation of convective inhibition (CIN) (Varga & Breuer, 2022). It also tends to overestimate weak precipitation events while underestimating strong precipitation events (Jiang et al., 2021). Additionally, ERA5 generally underestimates wind speed, although overestimations can also occur (Zhai et al., 2023). These factors collectively introduce unavoidable biases in the representation of environmental fields. However, recent studies have pointed out that the trend of precipitation variance shifting toward smaller scales in ERA5 is an artificial phenomenon caused by the gradual transition from parameterized to explicitly resolved convection over tropical oceans (Buschow, 2024), indicating that ERA5 continues to make efforts to reduce parameterization errors. Moreover, these biases are largely systematic across regions, and there is no evidence of regionally heterogeneous errors that would alter the comparative conclusions in this study. The key patterns and spatial contrasts remain robust despite these known uncertainties (Taszarek et al., 2021).

To ensure consistency and justify the use of environmental variables from ERA5, we will discuss the comparative study between ERA5 surface precipitation and GPM precipitation data. For the mainland China area, GPM precipitation products generally perform better than ERA5 precipitation products (Xu et al., 2022). Model-based products tend to underestimate the average precipitation rate of events, but ERA5 performs better than ERA-Interim and MERRA2, offering certain advantages among current reanalysis products (Gao et al., 2020). In the South China region, ERA5 performs better on a daily scale compared to PERSIANN-CCS and FY-4A. It must be acknowledged that ERA5 surface precipitation data lags behind GPM precipitation data in many aspects. However, this study aims to link the microphysical characteristics of rain cells with large-scale environmental conditions over an 8-year period, and using radiosonde data would reduce the sample size. Furthermore, some studies have already used these two data sets for research, demonstrating their feasibility (Sun et al., 2024). Therefore, we have decided to match ERA5 environmental data with GPM precipitation data for our analysis.

Some studies have suggested that strong convection is unlikely to occur when CAPE is below 800 J/kg, and we adopt this threshold as one of the criteria for identifying strong convection in this study (Emanuel, 2023). However, intense convective storms can still develop under relatively low CAPE conditions (Schneider & Dean, 2008), and high CAPE values do not necessarily guarantee strong convection. Compared to CAPE, vertical velocity is a more direct indicator of convective strength (Kirkpatrick et al., 2011). Regarding updraft speed, studies have shown that for MCSs in the United States, the 90th percentile of the strongest updrafts reaches 8 m/s at 5 km altitude, 11 m/s at 10 km, and up to 15 m/s near the tropopause (Schneider & Dean, 2008). Other studies have reported that, at 850 hPa, strong convection near Jiangsu, China can exhibit updraft speeds of up to 1 m/s (Cui et al., 2023). These results highlight significant regional differences in updraft intensity and illustrate that "strong convection" remains a somewhat ambiguous term. Therefore, it is difficult to directly adopt thresholds from previous studies. In this paper, we use 800 J/kg CAPE and 0.5 Pa/s vertical velocity as our working criteria for defining strong convection.

2.2. Front Identification

According to the type of meteorological elements, such as temperature and wind, front identification methods can be divided into those based on thermal factors (Hewson, 1998) and those based on dynamic factors (Simmonds et al., 2012). There are many methods for front identification, such as an algorithm based on the frontogenesis function (Bluestein, 1986), the classic H98 algorithm (Hewson, 1998), which was later optimized (Berry et al., 2011; Catto et al., 2012), and an algorithm for dynamic diagnosis based on 10-m wind time changes (Schemm et al., 2015). Moreover, the height of the data, grid spacing, and threshold of the data set need to be appropriately selected. It is therefore important to acknowledge that no two frontal detection methods can expect to produce identical results (Parfitt et al., 2017). In South China, the oblique characteristics of fronts and the hilly terrain make it difficult to objectively identify fronts (Han et al., 2021).

Previous studies have subjectively identified frontal boundaries based on wind shear at 925-hPa (indicating significant changes in wind direction) and temperature gradients (Wu et al., 2020). Therefore, the frontal identification algorithm in this study integrated the 925-hPa wind shear with the H98 method in order to better adapt to the South China region, where Thermodynamic Front Parameter (TFP) represents the TFP in the classic H98

ZUO ET AL. 5 of 23

method (Hewson, 1998) and Dynamic Front Parameter (DFP) is a DFP defined by the authors. The position of the front is determined by combining temperature and wind observations in the 925-hPa layers. This approach simplifies front identification and prevents misjudgment of South China coastal linear convection systems as fronts when using the TFP alone. It also avoids including boundaries such as dry lines that are not sensitive to either TFP or DFP. After applying the scale-based filtering, outflow boundaries generated by mesoscale convective systems are also excluded. These distinctions are illustrated in the conceptual diagram in Figure 2a. The data height is selected at the 925 hPa level, as previous studies on frontal issues in the South China area also frequently use this level. Regarding the grid spacing, we chose the resolution of the ERA5 data itself, which corresponds to a grid spacing of 0.25°, approximately 25–30 km. For the rain cell partitioning, we divided the region into areas of 100 km each. With this grid spacing, the distinction and sensitivity are satisfactory. The choice of thresholds will be explained in detail later in the text. The specific formulas used are as follows:

$$DFP = -\nabla |\nabla v| \cdot \frac{\nabla v}{|\nabla v|} \tag{1}$$

$$TFP = -\nabla |\nabla t| \cdot \frac{\nabla t}{|\nabla t|}$$
 (2)

where v is the meridional wind speed, t represents temperature, ∇v is the meridional wind speed gradient, and ∇t is the meridional temperature gradient. We first analyze TFP, where $\frac{\nabla t}{|\nabla t|}$ represents the unit vector in the direction of ∇t , which, in this study, corresponds to the direction of the temperature gradient, pointing either north or south. $\nabla |\nabla t|$ denotes the Laplacian of temperature, which describes the rate of change of the temperature gradient in the meridional direction. Its maximum value indicates the point where the temperature gradient increases at the fastest rate, whereas its minimum value indicates the point where the temperature gradient decreases at the fastest rate. For a cold front, the frontal boundary is typically defined near the warm air side, corresponding to the minimum value corresponding to $\nabla |\nabla t|$. At this location, the Laplacian of temperature, $\nabla |\nabla t|$, reaches its minimum value. Therefore, to ensure that the TFP reaches its maximum at the frontal position, we introduce a negative sign in the final formula. Similarly, in DFP, $\frac{\nabla v}{|\nabla v|}$ represents the direction of the meridional wind speed gradient, pointing either north or south, whereas $\nabla |\nabla v|$ denotes the Laplacian of the meridional wind speed, describing the rate of change of the meridional wind gradient in the north-south direction. Its maximum value indicates the point where the meridional wind gradient increases at the fastest rate, whereas its minimum value indicates the point where the meridional wind gradient decreases at the fastest rate. After testing, the criterion for determining a front is that both TFP and DFP must be greater than 0.3. The threshold of 0.3 for TFP is based on previous studies, particularly Hewson, who suggested this value as a universal criterion for identifying frontal zones at different altitude levels (Hewson, 1998). In contrast, the threshold for DFP was determined through our testing by evaluating different values. We found that 0.3 provided the best balance in identifying continuous and well-defined fronts while avoiding misclassification caused by cold pool boundaries from intense precipitation, which were excluded due to their limited horizontal extent and confinement to the near-surface layer (typically below 350 m) (Mai et al., 2025), whereas our analysis is based on the 925 hPa level (~700-800 m). Validation against surface weather charts from April to June 2015 further confirms the robustness of this threshold, with a Critical Success Index (CSI) of 0.82, outperforming thresholds of 0.2 (CSI = 0.29) and 0.4 (CSI = 0.06). This conclusion is also supported by our quantitative evaluation, which shows that a threshold of 0.3 yields the most balanced performance across multiple metrics such as hit rate and false alarm rate.

If the two points are separated by less than 2°, fronts comprising less than three points are removed. The majority of pre-summer rainfall in South China is generated by mesoscale convective systems along cold fronts or quasi-stationary fronts (Ding, 1994; Huang et al., 1986). The Nanling Mountains, situated at the coordinates of 23°30′–27°00′ N and 108°40′–116°20′ E, are located at the junction of five provinces in South China: Hunan, Jiangxi, Guangxi, Guangdong, and Fujian. It stretches approximately 850 km from east to west and 350 km from north to south (Huang et al., 2023). When these fronts cross the Nanling Mountains, they move slowly, and their characteristics gradually weaken. This criterion may eliminate some fuzzy fronts. In conclusion, since multiple grid points within a frontal zone may meet the above thresholds, potentially resulting in a certain north-south thickness of the front, we used a quadratic function fitting method to ensure the uniqueness of the front. This approach ultimately provides a mathematical expression for the frontal position. Two fronts with close timing are shown in

ZUO ET AL. 6 of 23

Figure 2. It can be observed that the frontal positions determined using only the TFP generally have a larger curvature, aligning with the temperature field distribution. This results in a large number of rain cells near the western boundary being included in the statistics, though they are actually located at the border between Guangxi and Guizhou, with different microphysical characteristics from South China (Chen et al., 2021). On the other hand, the frontal positions determined using only the DFP are generally shorter, aligning with the near-surface wind field distribution. This leads to a number of South China rain cells being excluded, resulting in an insufficient sample size. Therefore, we ultimately use a combination of both parameters for frontal identification.

2.3. Rain Cell Identification

In this study, the precipRateNearSurface data of GPM-2ADPR were first converted into binary data (0 for no rain and 1 for rain), and then rain cells were identified by a connected domain identification algorithm (Parodi et al., 2011). A rain cell was defined as adjacent rain pixels with a near-surface rain rate of at least 0.4 mm h⁻¹. In addition, this had to be in more than four consecutive grids. All the initial rain cells were retained, regardless of the rain cell affected by truncation of the DPR swath. This RC identification method has been widely used in event-based precipitation and cloud research (Fu et al., 2020). The vertical structure of terrestrial and marine rain cells differ greatly (Nesbitt et al., 2006). As such, only terrestrial rain cells were selected to study the differences in their microphysical parameters. Additionally, the centroid of the rain cells and the longitudinal and latitudinal positions of the data points contained in each rain cell were obtained.

2.4. Matching

In this step, the processed rain cell data and front data were matched to identify the distance between the centroid of each rain cell and the front. Since rain cells are not always scanned on the hour, they cannot fully correspond temporally to the front identification results provided by ERA5. More importantly, due to the blocking effect of the Nanling Mountains, the cold front slows down or even stops after passing over the mountains (Chen & Zhang, 2021). Consequently, an appropriate expansion of the temporal matching range will not affect the final result. Figure 2 illustrates the results of frontal identification and the changes in large-scale circulation within a three-hour period. At 14:00 local time, influenced by warm advection ahead of the front and local heating, the near-surface air temperature ahead of the front is relatively high (Figure 2b). Because of cold advection and cloudy weather behind the front, the near-surface temperature is lower, with a temperature difference of about 8 K between the north and south sides of the front (Figure 2b). Influenced by the Nanling Mountains, 3 hours later, the front has only moved southward by 0.2° in latitude, at 17:00 local time (Figure 2c). At this time, the temperature contrast has weakened but the frontal structure remains, and there is little change in the wind field. This indicates that matching a clear front at a specific time with rain cells 3 hours before and after will not affect the classification results of rain cells. This is because fronts move very slowly near South China, with movement of only about 20 km in 3 hours, which is much smaller than the 100 km interval used for zoning in this study. Moreover, objective criteria for frontal identification will exclude some weak fronts, and appropriately expanding the matching range will help increase the number of rain cells involved in classification. This helps avoid too few rain cells being matched due to frontal exclusion, thus enhancing the representativeness of the study samples. Here, the time range was set to 6 hours around the scan time of rain cells to find the closest front data for matching. Finally, fronts corresponding to rain cells were identified and classified into four areas—namely, 0–100 km (A), 100– 200 km (B), 200–300 km (C), and >300 km (D)—and the quantities of fronts in these areas were 78, 62, 46, and 54, respectively. The frontal positions in different panels do not correspond to the same front but instead represent rain cells at different distances ahead of various fronts, illustrating the variability in precipitation structures at different frontal distances. We also present plan views of typical rain cells and the near-surface wind field in each area to better observe their horizontal characteristics (Figure 3). We found that all four areas have grid points where the rain intensity exceeds 10 mm/hr, but the proportion of heavy rainfall and the organization of rain cells vary. The rain cells in areas A and C are more organized, with a large proportion of heavy rainfall. In area A, the rain cells exhibit a clear banded structure (Figure 3a), whereas in area C, they are more block-like (Figure 3c). In contrast, precipitation is scattered in areas B and D, with area B showing widespread weak rainfall and area D showing small areas of heavy rainfall (Figures 3b and 3d).

ZUO ET AL. 7 of 23

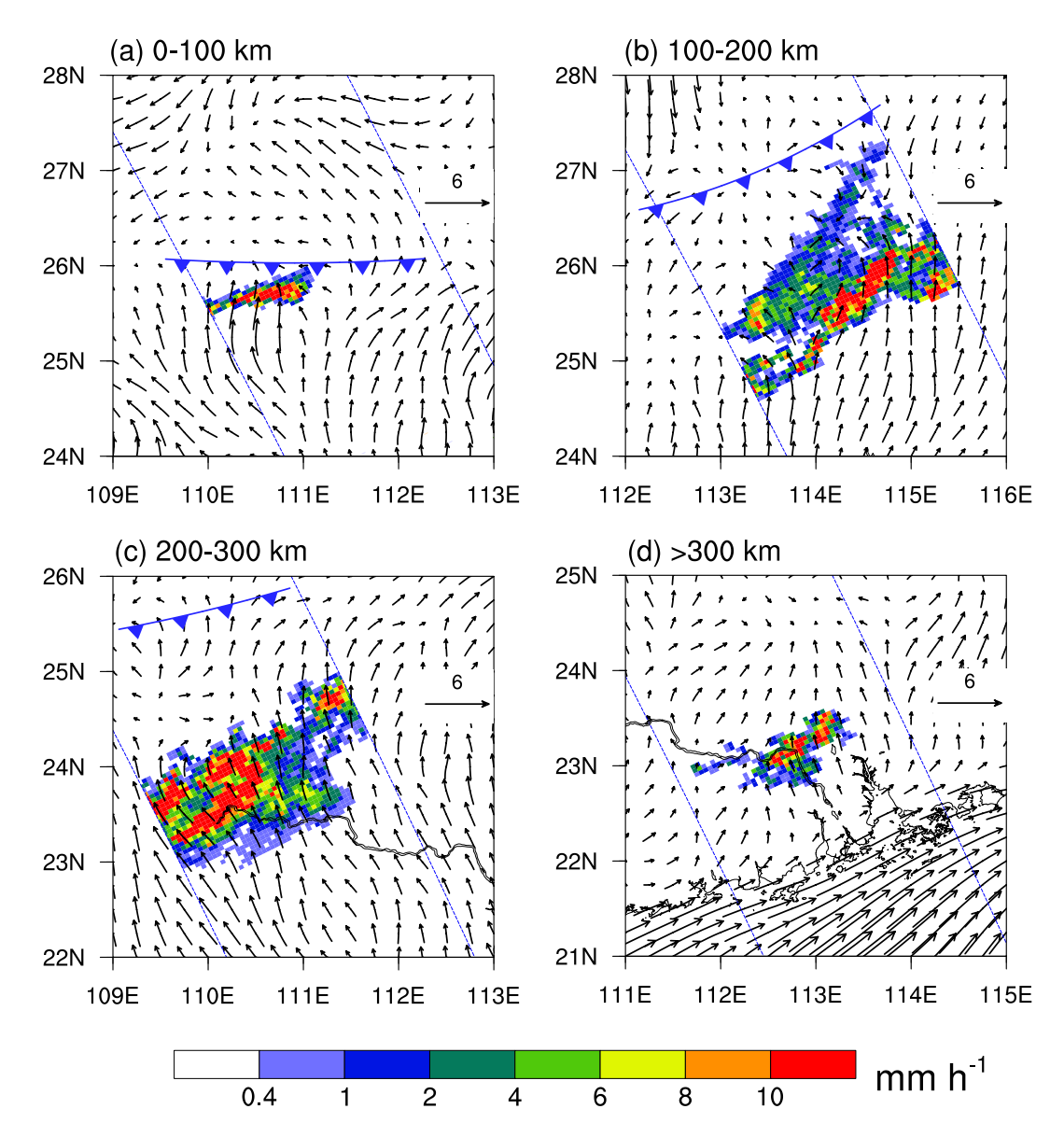


Figure 3. Demonstration of the horizontal patterns for the different classes of rain cells ahead of fronts: (a) 0–100 km; (b) 100–200 km; (c) 200–300 km; and (d) >300 km. The color scale indicates near-surface rain rate in mm/h. The overlapped arrows indicate the ERA5 10 m wind. The blue diagonal lines represent the edges of the DPR swaths. Dark blue lines represent the frontal positions. The frontal positions in different panels do not correspond to the same front but instead represent rain cells at different distances ahead of various fronts, illustrating the variability in precipitation structures at different frontal distances.

3. Results

Previous studies have extensively examined the large-scale environment around frontal zones during the presummer rainy season in South China. Behind the front, a dry northerly airflow dominates, while ahead of the front, a warm and moist southerly airflow prevails (Han et al., 2021). Additionally, low-level and boundary layer jets frequently occur ahead of the front, enhancing warm-moist air transport (Liu et al., 2022). The following summarizes the environmental and precipitation microphysical characteristics of areas A–D ahead of the front, integrating previous studies with this research.

The front's low-level dynamic forcing primarily affects its rear but extends into area A, where strong uplift occurs, with a maximum velocity exceeding -1.5 Pa/s (Figure 7d). Area B also experiences uplift, but it is weaker and peaks at 300 hPa (-1.1 Pa/s). High-altitude westerly winds influence areas 200–300 km ahead of the front,

ZUO ET AL. 8 of 23

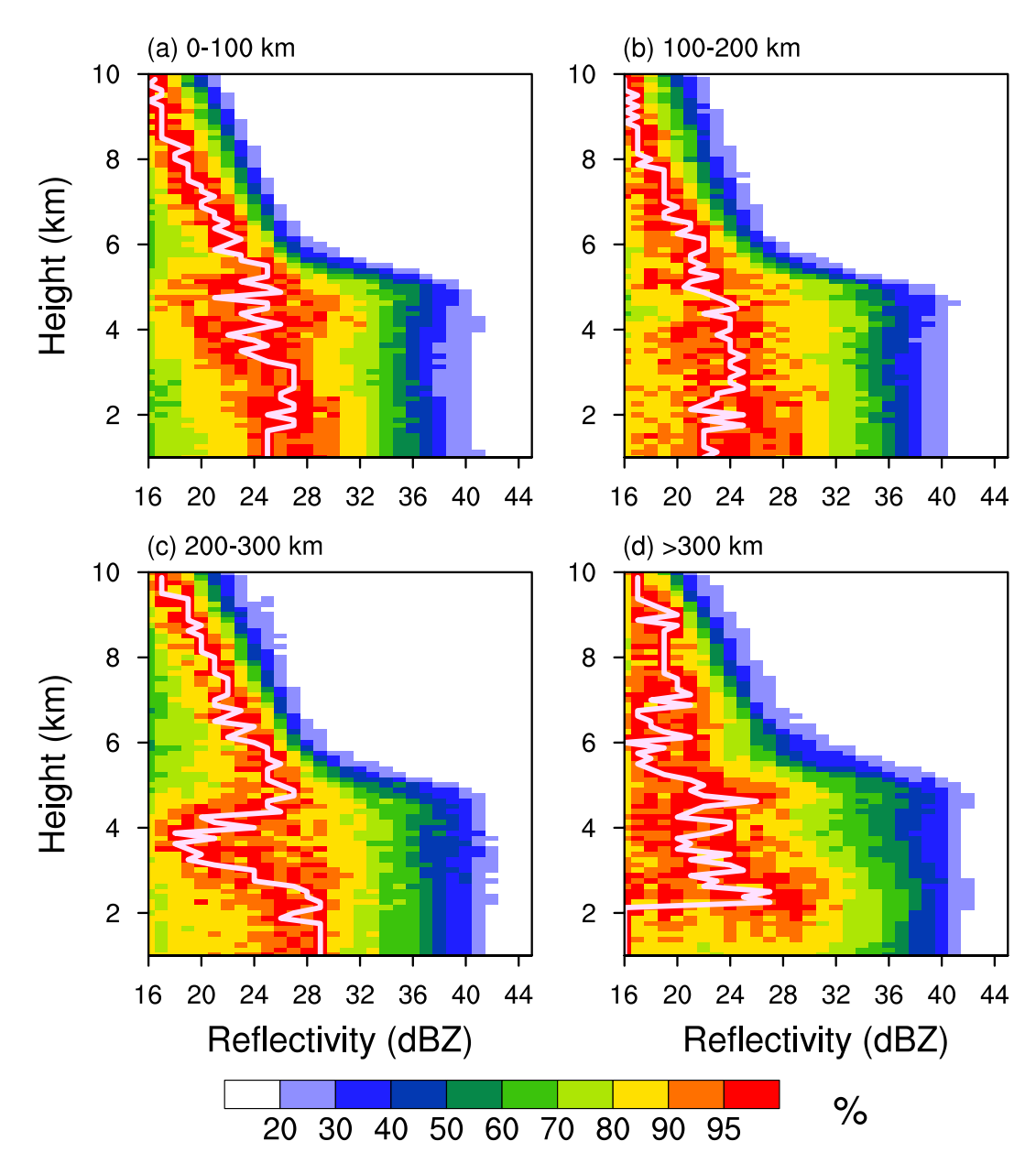


Figure 4. A contoured frequency by altitude diagram showing the frequency of occurrence of values of reflectivity at different heights for the rain cells in different areas in this study, which were normalized by the maximum bin values of each height level. The data exclude the shallow part, and the maximum value of each layer is represented by the white line.

impacting areas A–C (Figure S1c in Supporting Information S1). Among them, areas B and C exhibit the strongest divergence at 200 hPa, with a maximum of $2.8 \times 10^{-5} \, \mathrm{s}^{-1}$. In terms of thermodynamic conditions, CAPE is lowest in area A due to cold air penetration from the front, whereas area D exhibits the highest CAPE (>1300 J/kg, Figure S3d in Supporting Information S1). Precipitation frequency exceeds 80% in area A but is most intense in area C, whereas precipitation in areas B and D remains below 3.7 mm/hr on average (Figure 10). All four areas are dominated by stratiform precipitation, but convective precipitation proportions vary: 14.28%, 11.68%, 18.97%, and 17.89% in areas A, B, C, and D, respectively. The classification is based on the typePrecip variable from Level 2 DPR data, with convective and shallow convective precipitation ratios calculated as the number of respective grid points divided by the total number of rain cell grid points in each area.

Statistical analysis supports significant differences between areas B and C, as well as between areas B and D (p < 0.05). Despite being adjacent, areas B and C show notable variation in convective precipitation proportions,

ZUO ET AL. 9 of 23

com/doi/10.1029/2024JD043270 by Yilun Chen - Zhongshan University , Wiley Online Library on [27/10/2025]. See the Terms

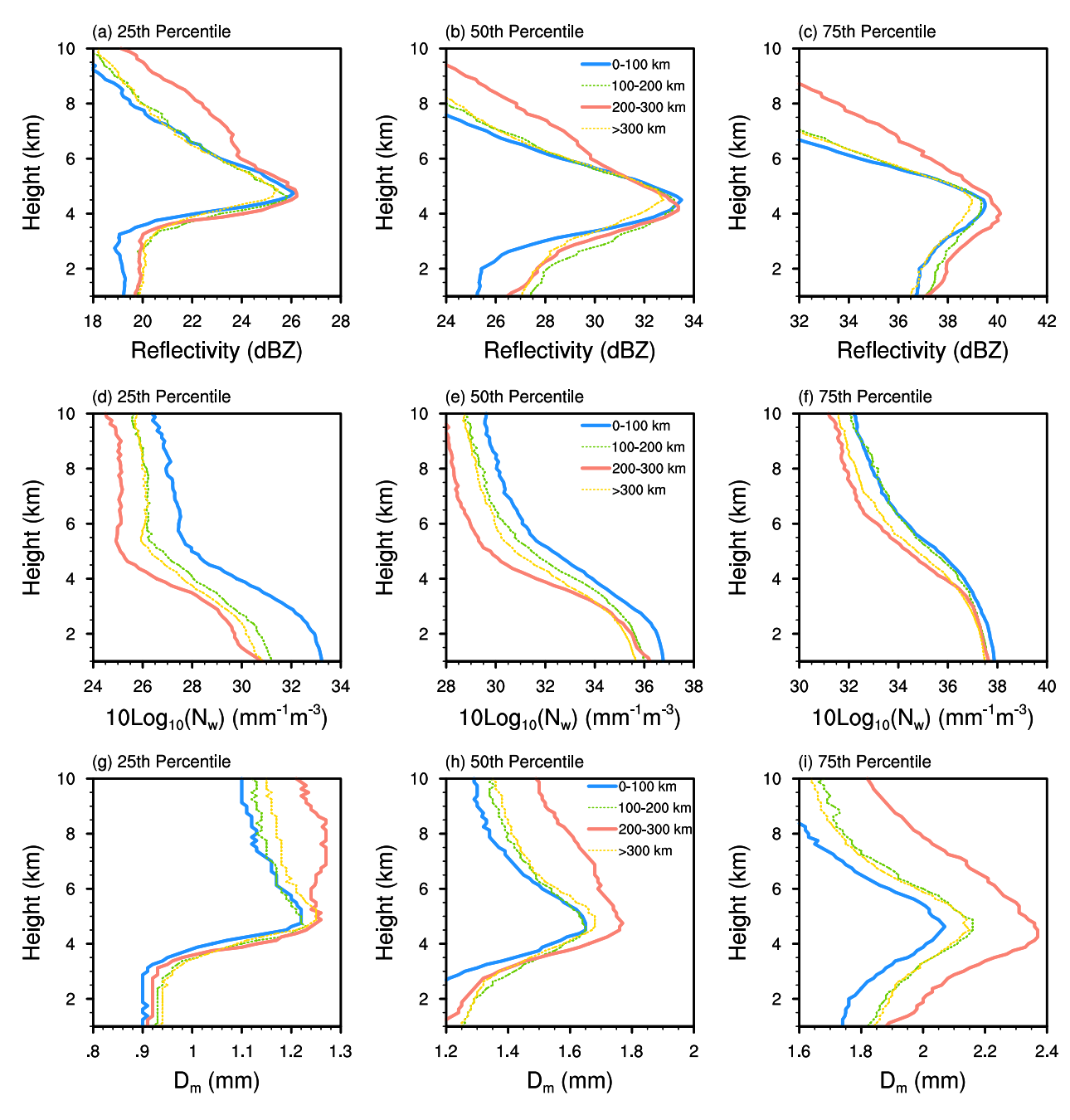


Figure 5. Vertical profiles of the median reflectivity, N_w and D_m for convective precipitation in the four areas. Profiles of the 25th to 75th percentile are shown in the left, middle, and right panels, respectively.

with area C (18.97%) exceeding area B (11.68%). Figure 3 further illustrates the spatial distribution of rain cells at different distances ahead of the front, showing variations in near-surface rain rates. This may be attributed to warmer, more humid conditions to the south (Crook, 1996; Sherwood et al., 2010). However, convective precipitation is also influenced by atmospheric stability, external triggering mechanisms, and moisture transport strength (Bai et al., 2021; Hirt et al., 2020; Schumacher & Rasmussen, 2020).

Microphysical properties vary among the four areas. Area C has the highest radar reflectivity (p < 0.05, Cohen's d = 0.4849), exceeding that in areas B and D (Figure 5c). It also exhibits the largest raindrop sizes, with significant differences from the other three areas (p < 0.05, Cohen's d = 0.8088). Area A shows the highest median raindrop concentration, though the difference is not statistically significant (p = 0.258, Cohen's d = 0.237), except

ZUO ET AL. 10 of 23

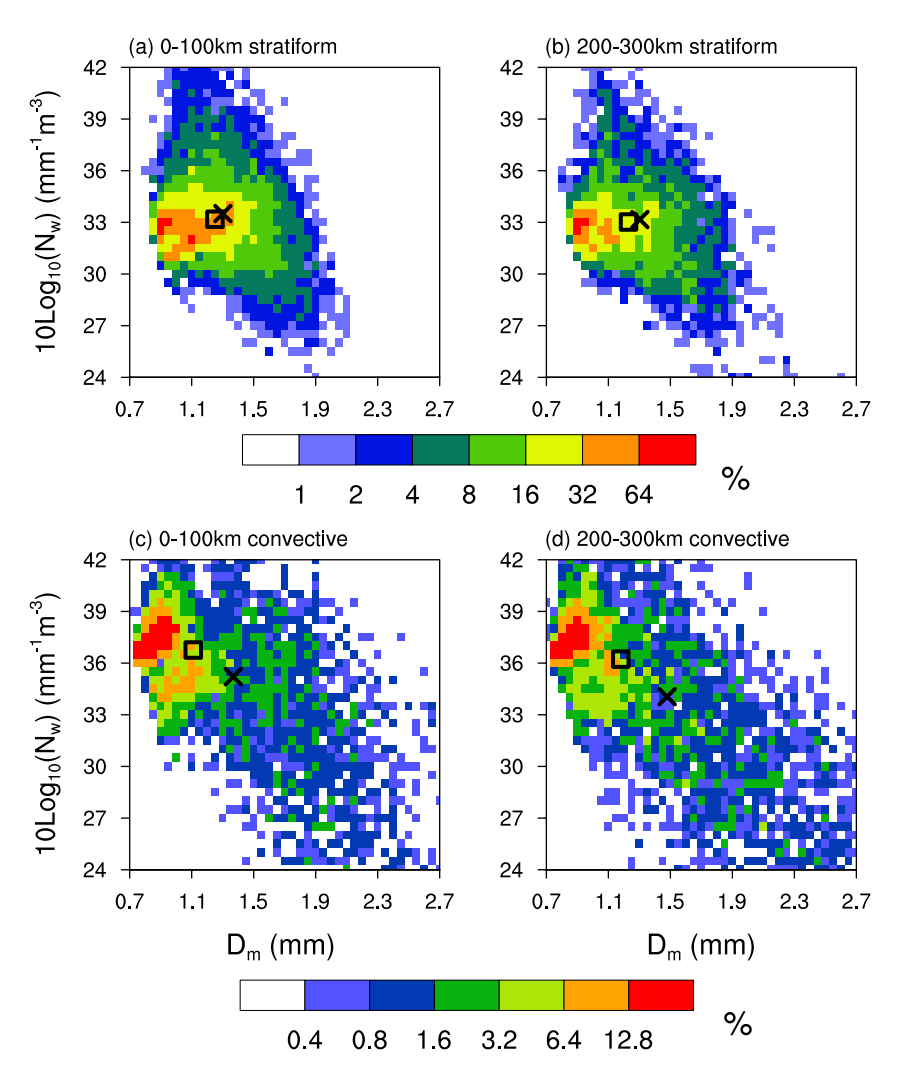


Figure 6. Distribution map of N_w and D_m at a height of 1 km from the ground, normalized by the overall maximum. Panels (a), (b), (c), and (d) represent stratiform precipitation in the 0–100 km range, stratiform precipitation in the 200–300 km range, convective precipitation in the 0–100 km range, and convective precipitation in the 200–300 km range from the front, respectively. The squares in each panel represent the median, whereas the multiplication sign represents the average.

at the 25th percentile (Figure S2d in Supporting Information S1). Further details are provided in the following sections, where all discussed data refer to median values unless otherwise specified.

3.1. Differences in Rainfall Microphysical Characteristics of Rain Cells

Rainfall intensity is stronger in areas A and C but weaker in areas B and D, with a difference of 1.4 mm/hr (Figure 10). In areas A and C, the frequency exceeding 90% is confined to a narrower reflectivity range (24–30 dBZ) compared to areas B (20–30 dBZ) and D (18–30 dBZ) (Figures 4a and 4c). This suggests a low degree of variability in radar reflectivity for rain cells in areas A and C, and the vertical precipitation structures within each area are consistent. The reflectivity in area A increases continuously above 4 km but stabilizes below, suggesting predominant stratiform precipitation. In contrast, area C exhibits both stratiform and convective precipitation, implying that its heavy rainfall results from both types.

In all areas, most high-frequency occurrences fall below 30 dBZ. However, areas B and D show a broader high-frequency reflectivity range (~14 dBZ at 2 km), over twice that of areas A and C (~6 dBZ), reflecting great variability and weak precipitation intensity (Figure 10). Area B features weak stratiform precipitation, with reflectivity increasing from 17 dBZ at 8 km to 24 dBZ at 5 km, then stabilizing (Figure 4b). Area D shows

ZUO ET AL. 11 of 23

om/doi/10.1029/2024JD043270 by Yilun Chen - Zhongshan University , Wiley Online Library on [27/10/2025]. See the Terms

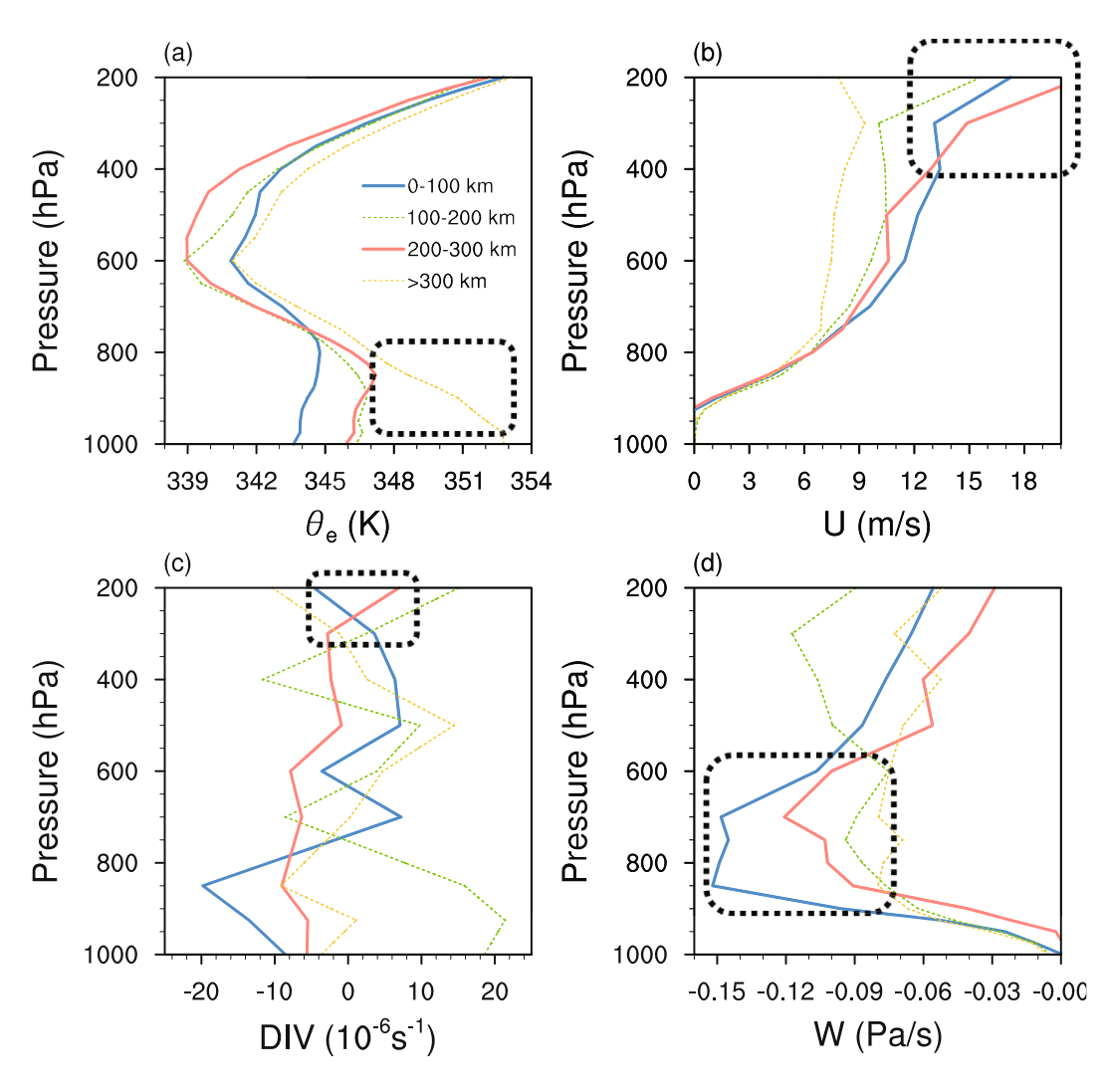


Figure 7. Vertical profiles of the median equivalent potential temperature (θ_e), U-component of wind (U), Divergence (DIV), and vertical velocity (W). All data were collected 3 hours prior to the onset of precipitation.

minimal increase in reflectivity above 5 km, indicating limited upper-level precipitation development, whereas its varied reflectivity below suggests a mix of warm-cloud precipitation and drizzle (Figure 4d).

The white lines in Figures 4a–4d highlight precipitation characteristics. Frontal precipitation, typically dominated by stratiform processes with strong ice-phase growth (Han et al., 2021; Houze Jr, 2014b), is evident in areas A–C, where reflectivity increases from 17 dBZ at 10 km to $\geq 24 \text{ dBZ}$ at 5 km. WR, characterized by stronger convection and low-level liquid-phase growth (Han et al., 2021; Wu et al., 2020), is observed in areas C and D, where reflectivity intensifies below 4 km. It is worth noting that area C exhibits characteristics of both frontal and WR, with particularly strong convection reflected by updraft velocity exceeding 0.7 Pa/s and CAPE values above 900 J/kg. These hybrid features will be further analyzed in subsequent sections.

We will analyze the vertical microphysical characteristics of rain cells in the four areas by dividing them into two parts: stratiform and convective. The analysis of the stratiform portion can be found in Supporting Information S1 (Text S1). Below is the analysis of the convective portion. Detailed comparisons of the microphysical characteristics in areas A, B, and D, as well as relevant literature analyses (e.g., Feng et al., 2023; Han et al., 2021), are provided in Supporting Information S1 (Text S2). Areas A and C exhibit similar reflectivity in the mid-levels, but differences occur in the low and high layers. The median radar reflectivity at heights of 3–5 km in area A is 33.5 ± 13.4 dBZ, similar to that in area C (33.4 ± 13.9 dBZ), with maximum values exceeding 33 dBZ in both

ZUO ET AL. 12 of 23

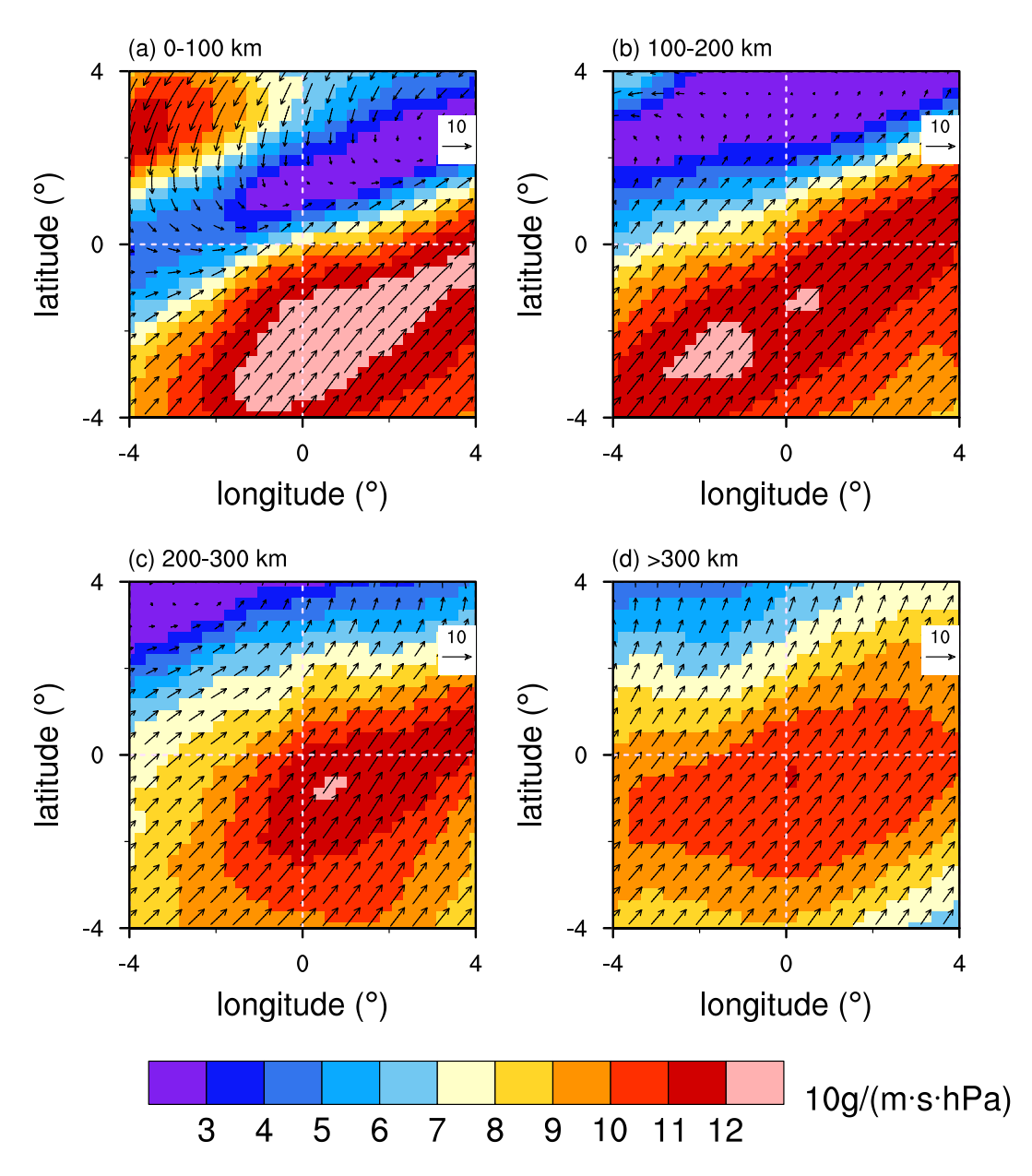


Figure 8. Horizontal distribution of the average U and V wind at 850 hPa. The shaded portion represents the intensity of moisture transport at 850 hPa. The figures are centered on the centroid of the rain cells, and four degrees of longitude or latitude are taken in each direction.

areas. However, differences are observed below 3 km and above 6 km (p < 0.05, Cohen's d = 0.9388), where the thickness of radar reflectivity greater than 26 dBZ in areas A and C are 5.5 and 8.5 km, respectively (Figure 5b).

From Figure 6, it can be observed that the near-surface raindrop size distribution in stratiform precipitation is relatively concentrated (Figures 6a and 6b), whereas the distribution in convective precipitation is relatively dispersed (Figures 6c and 6d). In areas A and C, the average raindrop concentration and size for stratiform precipitation are similar, with mean values around 33 mm⁻¹m⁻³ and 1.25 mm, respectively (Figures 6a and 6b), indicating that there are no notable differences between the two areas. But in area A, small raindrops between 1.1 and 1.5 mm can reach higher concentrations, with percentages reaching 2%–4% around 42 mm⁻¹m⁻³ (Figure 6a), whereas in area C, the proportion of raindrops of the same size is only 1%–2%, or even less than 1% (Figure 6b). For raindrops sized between 1.9 and 2.3 mm, the proportion is higher in area C than in area A but less than 4% (Figures 6a and 6b). This indicates that the stratiform precipitation in areas A and C is almost identical, but the

ZUO ET AL. 13 of 23

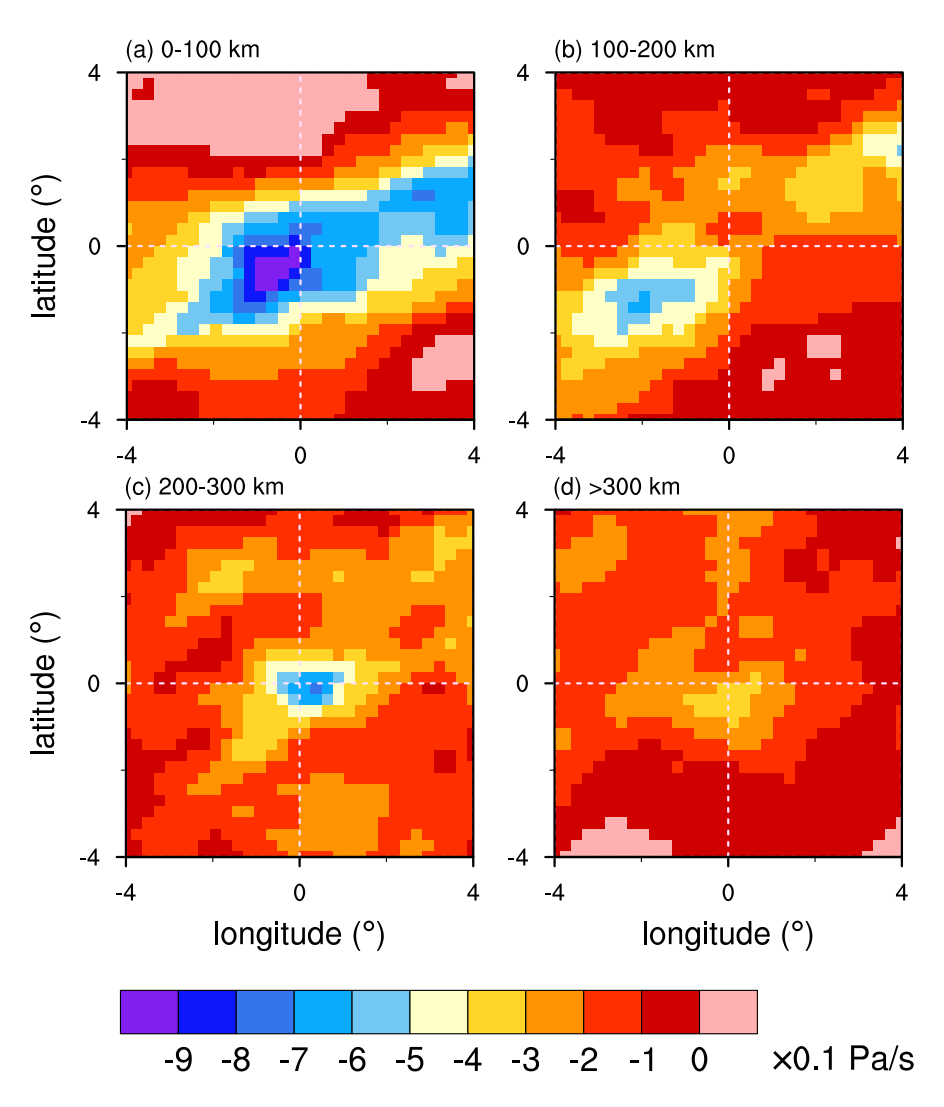


Figure 9. Same as Figure 8, but for average W wind at 850 hPa. Negative values represent updrafts; positive values represent downdrafts.

raindrops in area C are large and the low concentration due to the influence of a warm and humid environment (Figure 8c).

For convective precipitation, the differences between the two areas are not significant (p=0.988, Cohen's d=0.2366). The median and average raindrop concentrations in area A are higher than those in area C, with a difference of 3% (Figures 6c and 6d). Meanwhile, the raindrops in area C are larger than those in area A, being 8% larger on average (Figure 6d). Additionally, area C has a higher proportion of raindrops between 2.3 and 2.7 mm, which is 26% larger compared to area A. This suggests that under the warm and humid conditions in the south, both stratiform and convective precipitation tend to produce large raindrops, which may be related to the enhanced collision-coalescence process of raindrops.

3.2. Possible Reasons for the Microphysical Differences

The vertical profiles of equivalent potential temperature, wind, and vertical velocity reveal differences in stratification, wind patterns, and updraft speeds among areas A, B, C, and D, influencing their respective convective developments. According to the vertical profiles of equivalent potential temperature (Figure 7a), areas A and B are characterized by a stable stratification below 800 hPa and 900 hPa, respectively; area C has a similar low-level equivalent potential temperature distribution as area B; and area D possesses an unstable stratification below 600 hPa with a higher equivalent potential temperature near the ground, exceeding the other areas by more than

ZUO ET AL. 14 of 23

6 K, indicating the most unstable energy among all areas (Holton, 1973). The U-wind reflects the fact that all rain cells are dominated by westerly wind (Figure 7b). In area D, the westerly winds are the weakest, with an average westerly wind speed of less than 9 m/s, showing differences compared to the other three areas (p < 0.05, Cohen's d = 0.5094). The westerly winds in the high levels of areas A to C are relatively strong, with the maximum average westerly wind speeds all exceeding 15 m/s. Additionally, above 800 hPa, the westerly winds in area C are stronger than in area D (p < 0.05, Cohen's d = 1.3886), with an average difference of 4.8 ± 4.2 m/s, indicating that area C is also influenced by the upper-level westerlies from the front (Figure 7b). This is because area D is located far ahead of the front, resulting in a reduced influence from the frontal system.

The divergence profiles differ significantly among the four areas (p < 0.05, Cohen's d = 0.8991). Below 800 hPa, divergence values in areas A, C, and D are negative, indicating predominant low-level convergence (Figure 7c). In contrast, area B exhibits low-level divergence, making convective initiation more difficult. In area C, upperlevel divergence appears above 300 hPa, with a maximum strength of 6.94×10^{-6} s⁻¹ (Figure 7c), second only to Region B. By comparison, area D shows upper-level convergence above 300 hPa, with the strongest divergence centered near 500 hPa (Figure 7c). Overall, area C features the most favorable combination of low-level convergence and upper-level divergence. The vertical velocity among the rain cells exhibits notable regional differences, with important implications for rainfall organization and intensity. In area A, the strongest updrafts are concentrated in the mid-to-lower troposphere, with peak speeds between 700 and 850 hPa, whereas in area B, the maximum vertical velocity appears near 300 hPa, likely reflecting frontal lifting processes (Figure 7d; Houze Jr, 2014a). A comparison between areas C and D further reveals that the updrafts in area C are significantly stronger in the mid-to-low levels, with peak magnitudes approximately 50% higher than those in area D. Among all environmental parameters, the vertical structure of updrafts is arguably the most fundamental factor influencing the initiation, development, and intensity of convective systems. Strong and sustained ascent in the lower and middle troposphere enhances vertical moisture transport and instability release, supports latent heat-driven feedback, and ultimately sustains organized convection. Therefore, the more vigorous updraft profiles observed in areas A and C are not merely correlated with stronger rainfall—they are the key dynamical drivers that underlie the regional differences in convective behavior.

To further understand the factors influencing precipitation characteristics in different areas, we analyzed the dynamic and thermodynamic conditions associated with rainfall processes. When the rain cells are closer to the southern coast, the liquid-phase process may strengthen due to the higher low-level humidity around the coastal area (Han et al., 2021), causing the average raindrop size in areas C and D to be larger than in the other areas. In addition to the contribution of increased water vapor at low levels, upper-level divergence may also partly enhance the development of convection from a dynamic perspective (Machado & Laurent, 2004). The frontal convection in area A is primarily triggered by wind convergence caused by low-level frontal intrusion (Figure 8a) and is associated with the strongest low-level updrafts, with the maximum upward velocity exceeding -0.9 Pa/s (Figure 9a). Compared to the other three areas, area A has the lowest CIN and the lowest low-level equivalent potential temperature, with values ranging from 20 to 30 J/kg and 343.5 K, respectively. Additionally, area C has an equivalent potential temperature comparable to that of area B. Therefore, strong low-level updrafts and low-level moisture likely dominate the rainfall processes in areas C and D, resulting in large average raindrop sizes in the WR of these areas compared to the average raindrop sizes in the FR of area A. To better illustrate the distribution of westerlies at different distances ahead of the front, further analysis was conducted. Please refer to Text S3 in Supporting Information S1 for more details.

To examine the influence of wind patterns and moisture transport on precipitation characteristics, we analyzed the wind field and convergence zones in different areas. Figure 8a shows the presence of wind speed convergence along the frontal boundary in areas A and B. On the northern side, there is a northerly wind, a weak wind zone in the middle, and a southwesterly wind on the southern side, with the maximum average meridional winds exceeding 10 m/s. In areas A, B and C, the southwesterly winds around the rain cell centers gradually strengthen as they move away from the frontal boundary, with a cumulative increase exceeding 3 m/s (Figures 8a–8c). The maximum intensity of moisture transport in area D is approximately 10 g/(m·s·hPa) lower than that in area C (Figures 8c and 8d). Additionally, a low-level convergence zone caused by a noticeable decrease in wind speed can be observed in areas A, B, and C, but this feature is absent in area D. Figure 3 illustrates the wind field patterns at different distances from the front, showing how the convergence zones evolve with the movement of rain cells. Studies have shown that the convergence of warm, moist air associated with a low-level jet can trigger and support convection, which is further intensified by the release of latent heat, thereby extending the lifespan of mesoscale

ZUO ET AL. 15 of 23



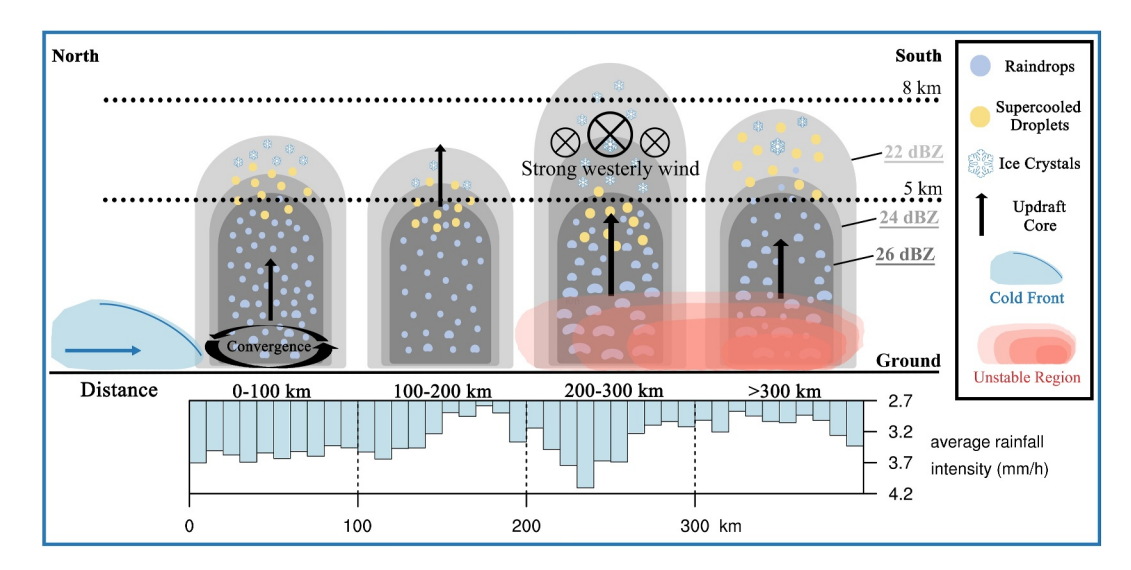


Figure 10. Conceptual model of the different precipitation microphysical characteristics among rain cells in different areas and the possible influential factors of the environment. The lower part of the picture shows the average precipitation intensity at different frontal distances on the 112° line of longitude obtained using Integrated Multi-satellitE Retrievals for GPM data. The calculation process excluded cases of no precipitation.

convective systems (Xu et al., 2017). This suggests that convective development in area D is suppressed, which is consistent with the weak precipitation observed in this area.

To better understand the vertical motion characteristics of rain cells in different areas, the updraft distributions at the 850-hPa level are analyzed. Figure 9a indicates that, at the 850-hPa level, there is a pronounced updraft near the center of the rain cell in area A, with the maximum upward velocity exceeding -0.9 Pa/s. The rain cells in area A are influenced by dynamic lifting near the frontal boundary, resulting in faster updraft speeds. For area B, there is also a peak in updraft speed (Figure 9b), but it is located away from the center of the rain cells, approximately 2° southwest of the rain cells' center, with the maximum updraft greater than -0.6 Pa/s. This may be because most rain cells in area B originate from area C, where favorable convective conditions lead to the development of distinct convective features. However, upon entering area B, unfavorable environmental factors hinder further development, resulting in weakened updrafts and gradual dissipation of the rain cells. Area A updrafts $(0.9 \pm 0.3 \text{ Pa/s})$ exceed area B $(0.6 \pm 0.2 \text{ Pa/s})$; Cohen's d = 1.012, p < 0.05).

In area C, the updraft strength is moderate, driven primarily by warm and moist conditions near the surface. Figure 9c shows that although there is a notable updraft within the rain cells, its spatial extent is relatively limited compared to area A. The updraft speed in area C is lower than that in area A, with a mean difference of 0.06 ± 0.22 Pa/s, indicating weaker convective development. The presence of these moderate updrafts suggests that convective activity in area C is still influenced by warm-sector conditions but is gradually transitioning toward a frontal influence as one moves closer to the boundary. This transitional nature supports the classification of the 200-300 km range as a distinct category, as rain cells in this area exhibit characteristics of both warm-sector and frontal precipitation.

In contrast, area D experiences the weakest updrafts among all areas. Figure 9d shows that the maximum updraft near the center of the rain cell remains below -0.4 Pa/s, with even weaker updraft speeds surrounding it. Area C updrafts (0.84 \pm 0.23 Pa/s) exceed area D (0.4 \pm 0.18 Pa/s; Cohen's d=1.865, p<0.05). This suggests the presence of a mechanism suppressing convective development in area D, despite the presence of high low-level instability. The suppressed updrafts indicate that area D lacks the necessary dynamic support for strong convection, distinguishing it from area C. This stark contrast between areas C and D further underscores the need to segment rain cells within the 200–300 km range as a separate category. The differences between these two areas demonstrate that area C retains some frontal influences, whereas area D is more representative of purely warm-sector conditions.

ZUO ET AL. 16 of 23

An analysis of upper-level wind and divergence fields provides insights into the atmospheric conditions supporting convection. Previous studies have indicated that upper-level divergence typically occurs in the exit region of strong upper-level winds (Zhang et al., 2024). Influenced by the frontal system, a strong westerly wind is observed in the mid to upper levels within 300 km ahead of the front, with the maximum westerly wind located near the frontal boundary and another peak between 200 and 300 km. The upper-level jet stream provides favorable upper-level divergence conditions that support the development of low-level convection, creating an optimal environment for the growth of rain cells. The divergence at 200 hPa near area B is the strongest, with the maximum average divergence reaching $2.8 \times 10^{-5} \text{s}^{-1}$. The strongest divergence in area B corresponds well with the peak vertical velocity appearing in the upper troposphere (around 300 hPa; Figure 7d), reflecting the vertical "suction" effect of upper-level divergence that enhances upward motion. Area C follows, with a maximum divergence of $2-2.4 \times 10^{-5} \text{s}^{-1}$. The upper-level divergence in areas A and D is weaker, with the maximum average divergence being less than $2 \times 10^{-5} \text{s}^{-1}$ (Figures S5a–S5d in Supporting Information S1).

In area A, although the updraft speed is the greatest in the low levels (Figure 9a), with the maximum upward velocity at 850 hPa approaching 1 Pa/s, the upper-level divergence is weak (Figure S5a in Supporting Information S1), and the low-level warm and moist conditions are insufficient, which hinders the sustained development of convection. Additionally, the low-level jet is crucial for triggering and organizing convective activity, forming severe storms, and causing heavy rainfall (Burrows et al., 2019). The westerly winds within the 200-300 km range are the strongest among the four areas (Figure S1a in Supporting Information S1), with the 75th percentile of 850-hPa westerly winds reaching 7-8 m/s. Additionally, there is strong divergence in the upper levels near area C (Figure S5c in Supporting Information S1). The combination of strong low-level southwesterly winds and strong upper-level winds forms a low-level convergence and upper-level divergence structure, which aids in the development of updrafts, providing favorable dynamic conditions for the formation of rain cells and their evolution into deep convective systems (Du & Chen, 2019; Pu et al., 2022). Beyond 300 km, the speed of the upper-level westerly wind decreases from above 10 m/s to below 10 m/s, and the low-level wind speed also decreases (Figure S1c in Supporting Information S1). Although certain upper-level divergence conditions exist (Figure S5d in Supporting Information S1), the upward velocity at 850 hPa in this area remains below -0.4 Pa/s, lower than in the other three areas where upward velocities exceed -0.6 Pa/s (Figure 9d), which is not conducive to the development of deep convective systems.

CAPE represents the specific amount of energy available for convection for a parcel of air. High values of CAPE generally indicate an unstable atmosphere with potential for upward motion, and extreme values are observed in thunderstorms and other severe weather systems. Lifted parcels will also often encounter a region where they become negatively buoyant and sink back down to the surface. The specific and vertically integrated amount of energy that causes this negative buoyancy is referred to as CIN (Früh & Wirth, 2007; Zhang, Short Gianotti, & Entekhabi, 2023). CAPE has been widely used to quantify atmospheric instability or the positive buoyancy that would be experienced by a lifted parcel, whereas CIN represents the energy needed to lift a parcel to above the level of free convection. Thus, CIN provides a measure of the stability in the lower troposphere that often prevents deep moist convection from happening if it is too strong. Both CAPE and CIN directly affect the occurrence frequency and intensity of atmospheric convection and convective precipitation (Chen et al., 2020). More detailed discussions on CAPE and CIN can be found in Supporting Information S1, specifically in Text S4, as well as Figures S3 and S4 in Supporting Information S1. Additionally, detailed information on the phase boundary height in different areas is provided in Supporting Information S1, in Text S5 and Figure S6.

The above results indicate that stratiform precipitation dominates in all four areas, with varying intensities and proportions of convective precipitation interspersed. In area A, the low-level dynamic environment is more favorable, with convergence of meridional winds and strong low-level updrafts, but the moisture supply is the weakest. Upper-level divergence is offset from the center and relatively weak, resulting in strong convective development, though with height limitations. The precipitation characteristics are similar to those of FR. In area B, the upper-level dynamic environment is better, with strong upper-level updrafts, but the low-level dynamic conditions are weaker compared to area A, and the thermodynamic conditions are inferior to those in area C, which limits the convective development in this area.

Area C has certain low-level warm and humid conditions, and when combined with mid-level updrafts and upper-level divergence, strong convective systems can be stimulated and maintained more frequently. And importantly, area C has all the favorable conditions to generate strong convection, and may be the location most likely to

ZUO ET AL. 17 of 23

trigger WR. Although area D farthest ahead of the front has the best low-level warmth and humidity, it still cannot produce the strong convective precipitation (Figures 5a-5c), and this is possibly because area D is mainly controlled by the northwestern Pacific subtropical high from April to June (Guan et al., 2019), meaning the height of convective development is thus restricted to a certain extent (Short & Nakamura, 2000). The suppression effect of the subtropical high is twofold: on one hand, it induces anomalous downward motion and upper-level convergence, inhibiting vertical development (Feng et al., 2011); on the other hand, it weakens the westerly flow and the associated jet-induced divergence, especially at distances exceeding 300 km ahead of the front (Houze Jr, 2014a). As a result, area D tends to support only shallow convection, such as thermally driven systems (Yamaji et al., 2020), consistent with our findings that upward motion is weak and upper-level divergence is lacking in this area. These dynamical constraints help explain why strong convective precipitation is largely absent in area D, despite the presence of favorable surface thermodynamic conditions. The main findings on the microphysical differences of rain cells in the four areas and the possible influential factors of the environment are summarized in the schematic in Figure 10. Since the proportion of stratiform precipitation in each area exceeds 58%, whereas convective precipitation accounts for less than 20%, the particle distribution characteristics are primarily dominated by the stratiform process. The development height of the rain cells is strongly influenced by the relatively small proportion of convective precipitation, resulting in clear distinctions. The environmental characteristics represent the average features of each rain cell without distinguishing between convective and stratiform precipitation.

4. Discussion

It is worth noting that both stratiform and convective precipitation in area C show strong development. As shown in the results, radar reflectivity and DSD parameters both indicate more intense development of both stratiform and convective precipitation in area C. WR is typically characterized by deep warm cloud layers and a moist environment that facilitate condensation growth and collision-coalescence processes, leading to efficient warm rain formation (Feng et al., 2023). Studies have shown that extreme WR is primarily driven by these warm rain microphysical processes, where the lack of strong frontal lifting and the presence of high humidity favor sustained warm-cloud development (Pu et al., 2022). This aligns well with the characteristics of stratiform precipitation in area C, where warm rain processes are dominant.

In contrast, frontal precipitation often involves stronger large-scale forcing and more pronounced ice-phase microphysics due to lower-altitude lifting and enhanced mixed-phase processes (Han et al., 2021; Yang et al., 2024). In area C, although warm rain processes dominate, ice-phase processes are also active. These large drops are likely supported by ice-phase processes, possibly involving melting hail. This is consistent with previous studies showing that extreme WR can also involve substantial ice-phase contributions, where the melting of large ice particles enhances raindrop production (Chen et al., 2023; Li, Wan, et al., 2020).

However, microphysical processes vary across different environments. Some studies have found that active ice-phase processes and effective warm rain processes jointly contribute to the formation of high-concentration and large raindrops (Chen et al., 2022), suggesting that both mechanisms are important for heavy precipitation rather than one being clearly dominant. Additionally, pre-summer precipitation in southern China often features a complex interplay between warm rain and ice-phase processes, with their relative contributions varying across different cases (Luo et al., 2020). The findings in this study suggest that area C exhibits characteristics of both warm-sector and frontal precipitation, where efficient warm rain processes are accompanied by active ice-phase processes, leading to the dual development of liquid- and ice-phase precipitation.

This research statistically analyzes the co-development of ice-phase and liquid-phase processes in area C. Warm rain and cold rain microphysical processes fundamentally differ. Warm rain involves collision and coalescence of raindrops and cloud droplets, whereas cold rain involves ice-phase processes, where ice crystals grow through deposition, hail, and aggregation above 0°C, and raindrops form below 0°C through the melting of snow or ice particles (Gao et al., 2021). Ice-phase precipitation formation is complex, with strong convection transporting moisture from warm clouds to the upper convective region, where vigorous updrafts generate large amounts of liquid and solid hydrometeors (Chen et al., 2023). In this stage, rapid growth of ice crystals occurs through deposition, whereas aggregation converts falling snowflakes and ice crystals into large snowflakes, increasing the average particle size above 0°C (Figure 5h). The raindrop size in area C is significantly larger than in other areas, indicating that more snow and solid water may melt and grow through collision with raindrops.

ZUO ET AL. 18 of 23

Liquid-phase precipitation development primarily depends on low-level warm-humid conditions and ascending processes (Pu et al., 2022), with warm rain closely linked to strong precipitation (Han et al., 2021; Li, Luo, et al., 2020). In area C, maximum moisture transport at 850 hPa exceeds 120 g/(m·s·hPa) (Figure 8c), supporting the warm rain process. Enhanced low-level conditions further promote updraft development. Area C is the only region with strong non-tilted updrafts, with maximum vertical velocities exceeding -0.7 Pa/s (Figure 9c), favoring raindrop collection, intensifying the warm rain process, and increasing average raindrop sizes below 4 km (Figure 5i). The vertical profile of reflectivity further confirms active low-level growth processes.

Moreover, mixed-phase processes may also contribute to strong precipitation (Petersen & Rutledge, 2001; Xu, 2020). The mixed-phase process refers to the coexistence of supercooled liquid water and ice crystals above the 0°C level (Vidaurre & Hallett, 2009). But their development in area C is similar to that in other areas. The low reflectivity near stratiform precipitation bright bands (Figure S2b in Supporting Information S1) and the low maximum reflectivity near the 0°C layer in convective precipitation (Figure 5b) suggest minimal differences in mixed-phase thickness (Figure S6b in Supporting Information S1). Overall, area C provides favorable conditions for the co-development of ice-phase and liquid-phase processes. However, the specific mechanisms governing the transition between these processes, including the relative contributions of warm rain and ice-phase processes under different environmental conditions, require further investigation.

5. Summary and Concluding Remarks

This study applied 8 years of GPM-2ADPR and ERA5 reanalysis data to comprehensively investigate the convective activities and precipitation microphysical characteristics of rain cells at varying distances ahead of fronts in South China during the pre-summer rainy season. The vertical distributions of reflectivity, raindrop concentration, raindrop size, and related environmental fields of rain cells in four areas were analyzed and compared. The main conclusions can be summarized as follows:

- 1. The proportions of convective precipitation in the rain cells in areas A (0–100 km), B (100–200 km), C (200–300 km) and D (>300 km) are 14.28%, 11.68%, 18.97%, and 17.89%, respectively. The convective precipitation ratio of rain cells in areas B and C shows a significant difference (*p* < 0.05), which is related to the differences in thermal conditions.
- 2. The rain cells in area A have a higher number of smaller raindrops, whereas those in area C consist of fewer raindrops with larger sizes, consistent with many previous case studies. Additionally, the rain cells in area A exhibit clear FR characteristics, whereas area C has favorable conditions for strong convection and is most likely to trigger WR.
- 3. The rain cells in area C have both ice-phase and liquid-phase development mechanisms, and have larger raindrop sizes than those in area A, especially above the 0°C level, indicating higher convective development and a stronger ice-phase process in area C. The strong westerly winds in the upper levels of area C enhance divergence, promoting convection development. This is influenced by the secondary circulation ahead of the front
- 4. The main reasons for the suppression of convective precipitation in areas B and D are different: area B lacks low-level dynamical lifting, whereas area D is characterized by insufficient high-level divergence.

This study found that the rain cells in area C exhibit both ice-phase and liquid-phase development mechanisms, which may lead to more intense rainfall, helping to explain extreme precipitation events in the context of global warming. Furthermore, this finding sends an important message to the modeling community: this type of precipitation microphysics should be taken seriously. Special attention should be given to the coordinated development of microphysical processes in the upper and lower levels of precipitation within 200–300 km ahead of the front. Importantly, due to ground coverage limitations, previous studies based on ground radar observations have rarely touched on the microphysical characteristics of precipitation over the entire South China area, and studies using TRMM or GPM satellite data sets have not revealed the convective intensity and precipitation microphysical processes of rain cells at different distances ahead of fronts. In order to accurately predict the transformation and impact of complex precipitation types in the pre-summer rainy season of South China, it is necessary to have a deeper understanding of the microphysical structural differences between various precipitation areas ahead of the front, especially to perform objective classification.

ZUO ET AL. 19 of 23

21698996, 2025, 20, Downloaded from https://agupubs

on [27/10/2025]. See the

Conflict of Interest

The authors declare no conflicts of interest relevant to this study.

Data Availability Statement

The GPM-2ADPR data are available at Goddard Earth Sciences Data and Information Services Center (Iguchi & Meneghini, 2021). The GPM-IMERG data are available at Goddard Earth Sciences Data and Information Services Center (Huffman et al., 2023). The ERA5 data are available at Copernicus Climate Change Service Climate Data Store (Hersbach et al., 2023).

Acknowledgments

This study was jointly supported by the Guangdong Major Project of Basic and Applied Basic Research (Grant 2020B0301030004), the National Natural Science Foundation of China (Grant 42105068), the Innovation Group Project of the Southern Marine Science and Engineering Guangdong Laboratory (Zhuhai) (Grant 311022006), the Guangdong Major Project of Basic and Applied Basic Research (Grant 2024A1515011006), and the Southern Marine Science and Engineering Guangdong Laboratory (Zhuhai) (Grant SML2024SP013).

References

- Bai, L., Chen, G., Huang, Y., & Meng, Z. (2021). Convection initiation at a coastal rainfall hotspot in south China: Synoptic patterns and orographic effects. *Journal of Geophysical Research: Atmospheres*, 126(24), e2021JD034642. https://doi.org/10.1029/2021JD034642
- Berry, G., Reeder, M. J., & Jakob, C. (2011). A global climatology of atmospheric fronts. Geophysical Research Letters, 38(4). https://doi.org/10. 1029/2010GL046451
- Bluestein, H. B. (1986). Fronts and jet streaks: A theoretical perspective. In *Mesoscale meteorology and forecasting* (pp. 173–215). Springer. https://doi.org/10.1007/978-1-935704-20-1_9
- Burrows, D. A., Ferguson, C. R., Campbell, M. A., Xia, G., & Bosart, L. F. (2019). An objective classification and analysis of upper-level coupling to the great plains low-level jet over the twentieth century. *Journal of Climate*, 32(21), 7127–7152. https://doi.org/10.1175/JCLI-D-18-0891.1
- Buschow, S. (2024). Tropical convection in ERA5 has partly shifted from parameterized to resolved. *Quarterly Journal of the Royal Meteorological Society*, 150(758), 436–446. https://doi.org/10.1002/qj.4604
- Catto, J., Jakob, C., Berry, G., & Nicholls, N. (2012). Relating global precipitation to atmospheric fronts. Geophysical Research Letters, 39(10). https://doi.org/10.1029/2012GL051736
- Chandrasekar, V., & Le, M. (2015). Evaluation of profile classification module of GPM-DPR algorithm after launch. *IEEE International Geoscience and Remote Sensing Symposium (IGARSS)*, 5174–5177. https://doi.org/10.1109/IGARSS.2015.7326999
- Chen, G., Zhao, K., Lu, Y., Zheng, Y., Xue, M., Tan, Z.-M., et al. (2022). Variability of microphysical characteristics in the "21-7" Henan extremely heavy rainfall event. Science China Earth Sciences, 65(10), 1861–1878. https://doi.org/10.1007/s11430-022-9972-9
- Chen, G., Zhao, K., Wen, L., Yang, J., Zheng, Y., Xu, F., et al. (2023). Linking ice-phase microphysics to raindrop characteristics in deep convection: A warm-sector extreme rainfall case study in eastern China. *Earth and Space Science*, 10(2), e2022EA002697. https://doi.org/10.1030/2022EA002697.
- Chen, J., Dai, A., Zhang, Y., & Rasmussen, K. L. (2020). Changes in convective available potential energy and convective inhibition under global warming. *Journal of Climate*, 33(6), 2025–2050. https://doi.org/10.1175/JCLI-D-19-0461.1
- Chen, T., & Zhang, D. (2021). A 7-Year climatology of warm-sector heavy rainfall over south China during the pre-summer months. *Atmosphere*, 12(7), 914. https://doi.org/10.3390/atmos12070914
- Chen, X., Zhao, K., & Xue, M. (2014). Spatial and temporal characteristics of warm season convection over pearl river Delta region, China, based on 3 years of operational radar data. *Journal of Geophysical Research: Atmospheres*, 119(22), 12447–12465. https://doi.org/10.1002/2014id021965
- Chen, Y., Chen, T., Wang, L. Y., Li, S. Q., & Xu, J. (2019). A review of the warm-sector rainstorms in China. *Torrential Rain and Disasters*, 38(5), 483–493. https://doi.org/10.3969/j.issn.1004-9045.2019.05.010
- Chen, Y., Wang, X., Huang, L., & Luo, Y. (2021). Spatial and temporal characteristics of abrupt heavy rainfall events over southwest China during 1981–2017. *International Journal of Climatology*, 41(5), 3286–3299. https://doi.org/10.1002/joc.7019
- Crook, N. A. (1996). Sensitivity of moist convection forced by boundary layer processes to low-level thermodynamic fields. *Monthly Weather Review*, 124(8), 1767–1785. https://doi.org/10.1175/1520-0493(1996)124<1767:SOMCFB>2.0.CO;2
- Cui, X., Chen, M., Qin, R., Li, C., & Han, L. (2023). The roles of surface convergence line and upper-level forcing on convection initiation ahead of a gust front: A case study. *Journal of Geophysical Research: Atmospheres*, 128(3), e2022JD036921. https://doi.org/10.1029/2022JD036921
- Delrieu, G., Andrieu, H., & Creutin, J. D. (2000). Quantification of path-integrated attenuation for X-and C-band weather radar systems operating in mediterranean heavy rainfall. *Journal of Applied Meteorology*, 39(6), 840–850. https://doi.org/10.1175/1520-0450(2000)039<0840: OOPIAF>2.0.CO:2
- Ding, Y. (1994). In Monsoons over China. Kluwer Academic Publisher.419.
- Du, Y., & Chen, G. (2019). Heavy rainfall associated with double low-level jets over southern China. Part II: Convection initiation. *Monthly Weather Review*, 147(2), 543–565. https://doi.org/10.1175/MWR-D-18-0102.1
- Emanuel, K. (2023). On the physics of high CAPE. Journal of the Atmospheric Sciences, 80(11), 2669–2683. https://doi.org/10.1175/JAS-D-23-0060.1
- Feng, L., Hu, S., Liu, X.-T., Li, H.-Q., Xiao, H., Li, X.-H., et al. (2023). Comparison of microphysical characteristics between warm-sector and frontal heavy rainfall in the south of China. *Journal of Tropical Meteorology*, 29(1), 87–100. https://doi.org/10.46267/j.1006-8775.2023.007
- Feng, S., Liu, Q., & Fu, Y.-F. (2011). Cloud variations under subtropical high conditions. *Advances in Atmospheric Sciences*, 28(3), 623–635. https://doi.org/10.1007/s00376-010-9194-0
- Früh, B., & Wirth, V. (2007). Convective available Potential energy (CAPE) in mixed phase cloud conditions. Quarterly Journal of the Royal Meteorological Society: A journal of the atmospheric sciences, applied meteorology and physical oceanography, 133(624), 561–569. https://doi.org/10.1002/qj.39
- Fu, Y., Chen, Y., Zhang, X., Wang, Y., Li, R., Liu, Q., et al. (2020). Fundamental characteristics of tropical rain cell structures as measured by TRMM PR. *Journal of Meteorological Research*, 34(6), 1129–1150. https://doi.org/10.1007/s13351-020-0035-5
- Fu, Y., Pan, X., Xian, T., Liu, G., Zhong, L., Liu, Q., et al. (2018). Precipitation characteristics over the steep slope of the himalayas in rainy season observed by TRMM PR and VIRS. Climate Dynamics, 51(5–6), 1971–1989. https://doi.org/10.1007/s00382-017-3992-3
- Gao, W., Xue, L., Liu, L., Lu, C., Yun, Y., & Zhou, W. (2021). A study of the fraction of warm rain in a pre-summer rainfall event over south China. Atmospheric Research, 262, 105792. https://doi.org/10.1016/j.atmosres.2021.105792

ZUO ET AL. 20 of 23

- Gao, Z., Huang, B., Ma, Z., Chen, X., Qiu, J., & Liu, D. (2020). Comprehensive comparisons of state-of-the-art gridded precipitation estimates for hydrological applications over southern China. *Remote Sensing*, 12(23), 3997. https://doi.org/10.3390/rs12233997
- Guan, W., Hu, H., Ren, X., & Yang, X. (2019). Subseasonal zonal variability of the Western Pacific subtropical high in summer: Climate impacts and underlying mechanisms. Climate Dynamics, 53(5–6), 3325–3344. https://doi.org/10.1007/s00382-019-04705-4
- Han, B., Du, Y., Wu, C., & Liu, X. (2021). Microphysical characteristics of the coexisting frontal and warm-sector heavy rainfall in south China. Journal of Geophysical Research-Atmospheres, 126(21), 12. https://doi.org/10.1029/2021jd035446
- Hersbach, H., Bell, B., Berrisford, P., Biavati, G., Horányi, A., Muñoz Sabater, J., et al. (2023). ERA5 hourly data on single levels from 1940 to present [Dataset]. Copernicus Climate Change Service (C3S) Climate Data Store (CDS). (updated daily). https://doi.org/10.24381/cds.bd0915c6
- Hewson, T. D. (1998). Objective fronts. Meteorological Applications, 5(1), 37-65. https://doi.org/10.1017/s1350482798000553
- Hirt, M., Craig, G. C., Schäfer, S. A., Savre, J., & Heinze, R. (2020). Cold-pool-driven convective initiation: Using causal graph analysis to determine what convection-permitting models are missing. *Quarterly Journal of the Royal Meteorological Society*, 146(730), 2205–2227. https://doi.org/10.1002/qj.3788
- Holton, J. R., & Staley, D. O. (1973). An introduction to dynamic meteorology. *American Journal of Physics*, 41(5), 752–754. https://doi.org/10.1119/1.1987371
- Houze, R. A. J. (2014). Cloud dynamics. Academic Press. https://doi.org/10.1016/c2009-0-18311-3
- Houze Jr, R. A. (2014). Nimbostratus and the separation of convective and stratiform precipitation. In *International geophysics* (Vol. 104, pp. 141–163). Elsevier. https://doi.org/10.1016/B978-0-12-374266-7.00006-8
- Huang, H., Zhao, K., Fu, P., Chen, H., Chen, G., & Zhang, Y. (2021). Validation of precipitation measurements from the dual-frequency precipitation radar onboard the GPM core observatory using a polarimetric radar in south China. *IEEE Transactions on Geoscience and Remote Sensing*, 60, 1–16. https://doi.org/10.1109/TGRS.2021.3118601
- Huang, L., Yuan, L., Xia, Y., Yang, Z., Luo, Z., Yan, Z., et al. (2023). Landscape ecological risk analysis of subtropical vulnerable mountainous areas from a spatiotemporal perspective: Insights from the nanling Mountains of China. *Ecological Indicators*, 154, 110883. https://doi.org/10.1016/j.ecolind.2023.110883
- Huang, S., Li, Z., & Bao, C. (1986). Heavy rains in the first rainy season of south China (Vol. 230). Guangdong Science and Technology Press.
 Huffman, G. J., Bolvin, D. T., Braithwaite, D., Hsu, K. L., Joyce, R. J., Kidd, C., et al. (2020). Integrated multi-satellite retrievals for the global precipitation measurement (GPM) mission (IMERG). Satellite Precipitation Measurement, 1, 343–353. https://doi.org/10.1007/978-3-030-24568-9
- Huffman, G. J., Stocker, E. F., Bolvin, D. T., Nelkin, E. J., & Jackson, T. (2023). GPM IMERG final precipitation L3 half hourly 0.1 degree x 0.1 degree V07. Greenbelt. MD [Dataset]. Goddard Earth Sciences Data and Information Services Center (GES DISC). https://doi.org/10.5067/GPM/IMERG/3B-HH/07
- Huo, Z., Ruan, Z., Wei, M., Ge, R., Li, F., & Ruan, Y. (2019). Statistical characteristics of raindrop size distribution in south China summer based on the vertical structure derived from VPR-CFMCW. Atmospheric Research, 222, 47–61. https://doi.org/10.1016/j.atmosres.2019.01.022
- Iguchi, T., & Meneghini, R. (2021). GPM DPR precipitation profile L2A 1.5 hours 5 km V07. Greenbelt. MD [Dataset]. Goddard Earth Sciences Data and Information Services Center (GES DISC). https://doi.org/10.5067/GPM/DPR/GPM/2A/07
- Iguchi, T., Seto, S., Meneghini, R., Yoshida, N., Awaka, J., Kubota, T., et al. (2012). An overview of the precipitation retrieval algorithm for the dual-frequency precipitation radar (DPR) on the global precipitation measurement (GPM) mission's core satellite. Paper presented at the Earth Observing Missions and Sensors: Development, Implementation, and Characterization II, 8528, 250–256. https://doi.org/10.1117/12.977352
- Jiang, Q., Li, W., Fan, Z., He, X., Sun, W., Chen, S., et al. (2021). Evaluation of the ERA5 reanalysis precipitation dataset over Chinese mainland. Journal of Hydrology, 595, 125660. https://doi.org/10.1016/j.jhydrol.2020.125660
- Jin, D., Oreopoulos, L., Lee, D., Tan, J., & Cho, N. (2021). Cloud-precipitation hybrid regimes and their projection onto IMERG precipitation data. *Journal of Applied Meteorology and Climatology*(6). https://doi.org/10.1175/JAMC-D-20-0253.1
- Kirkpatrick, C., McCaul Jr, E. W., & Cohen, C. (2011). Sensitivities of simulated convective storms to environmental CAPE. *Monthly Weather Review*, 139(11), 3514–3532. https://doi.org/10.1175/2011MWR3631.1
- Kundzewicz, Z. W., & Pińskwar, I. (2022). Are pluvial and fluvial floods on the rise? Water, 14(17), 2612. https://doi.org/10.3390/w14172612
 Lavers, D. A., Simmons, A., Vamborg, F., & Rodwell, M. J. (2022). An evaluation of ERA5 precipitation for climate monitoring. Quarterly Journal of the Royal Meteorological Society, 148(748), 3152–3165. https://doi.org/10.1002/qj.4351
- Li, H., Wan, Q., Peng, D., Liu, X., & Xiao, H. (2020). Multiscale analysis of a record-breaking heavy rainfall event in Guangdong, China. Atmospheric Research, 232, 104703. https://doi.org/10.1016/j.atmosres.2019.104703
- Li, M., Luo, Y., Zhang, D.-L., Chen, M., Wu, C., Yin, J., & Ma, R. (2020). Analysis of a record-breaking rainfall event associated with a monsoon coastal megacity of south China using multisource data. IEEE Transactions on Geoscience and Remote Sensing, 59(8), 6404–6414. https://doi.org/10.1109/TGRS.2020.3029831
- Li, X., & Du, Y. (2021). Statistical relationships between two types of heavy rainfall and low-level jets in south China. *Journal of Climate*, 34(21), 8549–8566. https://doi.org/10.1175/jcli-d-21-0121.1
- Li, X., Zhang, K., Bao, H., & Zhang, H. (2022). Climatology and changes in hourly precipitation extremes over China during 1970–2018. Science of The Total Environment, 839, 156297. https://doi.org/10.1016/j.scitotenv.2022.156297
- Liu, H., Huang, X., Fei, J., Zhang, C., & Cheng, X. (2022). Spatiotemporal features and associated synoptic patterns of extremely persistent heavy rainfall over China. *Journal of Geophysical Research: Atmospheres*, 127(15), e2022JD036604. https://doi.org/10.1029/2022JD036604
- Liu, X., Luo, Y., Guan, Z., & Zhang, D. L. (2018). An extreme rainfall event in coastal south China during SCMREX-2014: Formation and roles of rainband and echo trainings. *Journal of Geophysical Research: Atmospheres*, 123(17), 9256–9278. https://doi.org/10.1029/2018jd028418
- Luo, Y., Xia, R., & Chan, J. C. (2020). Characteristics, physical mechanisms, and prediction of pre-summer rainfall over south China: Research progress during 2008–2019. *Journal of the Meteorological Society of Japan. Ser. II*, 98(1), 19–42. https://doi.org/10.2151/jmsj.2020-002
- Luo, Y., Zhang, R., Wan, Q., Wang, B., Wong, W. K., Hu, Z., et al. (2017). The southern China monsoon rainfall experiment (SCMREX). Bulletin of the American Meteorological Society, 98(5), 999–1013. https://doi.org/10.1175/bams-d-15-00235.1
- Machado, L. A. T., & Laurent, H. (2004). The convective system area expansion over Amazonia and its relationships with convective system life duration and high-level wind divergence. *Monthly Weather Review*, 132(3), 714–725. https://doi.org/10.1175/1520-0493(2004)132<0714: tcsaeo>2.0.co;2
- Mai, C., Du, Y., Li, M., Chen, G., Su, L., Li, C., et al. (2025). Cold pools detected by a 356-m meteorological tower in a monsoon coastal region. Advances in Atmospheric Sciences, 42(11), 1–12. https://doi.org/10.1007/s00376-025-4446-1
- Masaki, T., Iguchi, T., Kanemaru, K., Furukawa, K., Yoshida, N., Kubota, T., & Oki, R. (2020). Calibration of the dual-frequency precipitation radar onboard the global precipitation measurement core observatory. *IEEE Transactions on Geoscience and Remote Sensing*, 60, 1–16. https://doi.org/10.1109/TGRS.2020.3039978

ZUO ET AL. 21 of 23

- Nesbitt, S. W., Cifelli, R., & Rutledge, S. A. (2006). Storm morphology and rainfall characteristics of TRMM precipitation features. *Monthly Weather Review*, 134(10), 2702–2721. https://doi.org/10.1175/mwr3200.1
- Parfitt, R., Czaja, A., & Seo, H. (2017). A simple diagnostic for the detection of atmospheric fronts. Geophysical Research Letters, 44(9), 4351–4358. https://doi.org/10.1002/2017g1073662
- Parodi, A., Foufoula-Georgiou, E., & Emanuel, K. (2011). Signature of microphysics on spatial rainfall statistics. *Journal of Geophysical Research*, 116(D14), D14119. https://doi.org/10.1029/2010jd015124
- Petersen, W. A., & Rutledge, S. A. (2001). Regional variability in tropical convection: Observations from TRMM. *Journal of Climate*, 14(17), 3566–3586. https://doi.org/10.1175/1520-0442(2001)014<3566:RVITCO>2.0.CO;2
- Petracca, M., D'Adderio, L., Porcù, F., Vulpiani, G., Sebastianelli, S., & Puca, S. (2018). Validation of GPM dual-frequency precipitation radar (DPR) rainfall products over Italy. *Journal of Hydrometeorology*, 19(5), 907–925. https://doi.org/10.1175/jhm-d-17-0144.1
- Pu, Y., Hu, S., Luo, Y., Liu, X., Hu, L., Ye, L., et al. (2022). Multiscale perspectives on an extreme warm-sector rainfall event over coastal south China. *Remote Sensing*, 14(13), 3110. https://doi.org/10.3390/rs14133110
- Rao, X., Zhao, K., Chen, X., Huang, A., Hu, S., Hu, D., & Liu, X. (2022). Roles of multi-scale orography in triggering nocturnal convection at a summer rainfall hotspot over the south China Coast: A case study. *Journal of Geophysical Research: Atmospheres*, 127(12), 3. https://doi.org/10.1029/2022id036503
- Ryu, J., Song, H. J., Sohn, B. J., & Liu, C. (2021). Global distribution of three types of drop size distribution representing heavy rainfall from GPM/DPR measurements. *Geophysical Research Letters*, 48(3), 25. https://doi.org/10.1029/2020gl090871
- Schemm, S., Rudeva, I., & Simmonds, I. (2015). Extratropical fronts in the lower troposphere–global perspectives obtained from two automated methods. *Quarterly Journal of the Royal Meteorological Society*, 141(690), 1686–1698. https://doi.org/10.1002/qj.2471
- Schneider, R. S., & Dean, A. R. (2008). A comprehensive 5-year severe storm environment climatology for the Continental United States. In *Preprints*. 24th conf. On severe local storms. Amer. Meteor. Soc. A. https://doi.org/10.1175/0065-9401-28.50.433
- Schumacher, R. S., & Rasmussen, K. L. (2020). The formation, character and changing nature of mesoscale convective systems. *Nature Reviews Earth and Environment*, 1(6), 300–314. https://doi.org/10.1038/s43017-020-0057-7
- Seto, S., Iguchi, T., Meneghini, R., Awaka, J., Kubota, T., Masaki, T., & Takahashi, N. (2021). The precipitation rate retrieval algorithms for the GPM Dual-frequency precipitation radar. *Journal of the Meteorological Society of Japan. Ser. II*, 99(2), 205–237. https://doi.org/10.2151/jmsj.
- Sherwood, S., Roca, R., Weckwerth, T., & Andronova, N. (2010). Tropospheric water vapor, convection, and climate. *Reviews of Geophysics*, 48(2), 322. https://doi.org/10.1029/2009rg000301
- Short, D. A., & Nakamura, K. (2000). TRMM radar observations of shallow precipitation over the tropical oceans. *Journal of Climate*, 13(23), 4107–4124. https://doi.org/10.1175/1520-0442(2000)013<4107:troosp>2.0.co;2
- Simmonds, I., Keay, K., & Bye, J. A. T. (2012). Identification and climatology of southern hemisphere Mobile fronts in a modern reanalysis. *Journal of Climate*, 25(6), 1945–1962. https://doi.org/10.1175/jcli-d-11-00100.1
- Song, F., Zhang, G. J., Ramanathan, V., & Leung, L. R. (2022). Trends in surface equivalent potential temperature: A more comprehensive metric for global warming and weather extremes. *Proceedings of the National Academy of Sciences*, 119(6), e2117832119. https://doi.org/10.1073/pngs_2117832119
- Sun, N., Lu, G., & Fu, Y. (2024). Microphysical characteristics of precipitation within convective overshooting over east China observed by GPM DPR and ERA5. Atmospheric Chemistry and Physics, 24(12), 7123–7135. https://doi.org/10.5194/acp-24-7123-2024
- Sun, Y., Dong, X., Cui, W., Zhou, Z., Fu, Z., Zhou, L., et al. (2020). Vertical structures of typical meiyu precipitation events retrieved from GPM-DPR. *Journal of Geophysical Research: Atmospheres*, 125(1), e2019JD031466. https://doi.org/10.1029/2019JD031466
- Tao, S. Y. (1987). A review of recent research on the East Asian summer monsoon in China. Monsoon meteorology, 60-92.
- Taszarek, M., Pilguj, N., Allen, J. T., Gensini, V., Brooks, H. E., & Szuster, P. (2021). Comparison of convective parameters derived from ERA5 and MERRA-2 with rawinsonde data over Europe and North America. *Journal of Climate*, 34(8), 3211–3237. https://doi.org/10.1175/JCLI-D-20-0484.1
- Uijlenhoet, R., & Berne, A. (2008). Stochastic simulation experiment to assess radar rainfall retrieval uncertainties associated with attenuation and its correction. *Hydrology and Earth System Sciences*, 12(2), 587–601. https://doi.org/10.5194/hess-12-587-2008
- Varga, Á. J., & Breuer, H. (2022). Evaluation of convective parameters derived from pressure level and native ERA5 data and different resolution WRF climate simulations over central Europe. Climate Dynamics, 58(5), 1569–1585. https://doi.org/10.1007/s00382-021-05979-3
- Vidaurre, G., & Hallett, J. (2009). Ice and water content of stratiform mixed-phase cloud. *Quarterly Journal of the Royal Meteorological Society:*A journal of the atmospheric sciences, applied meteorology and physical oceanography, 135(642), 1292–1306. https://doi.org/10.1002/qj.440

 Wang, C., Hsu, H., & Chen, Y. (2021). Observed and projected frontal activities in east Asia. *Journal of Climate*, 34(8), 3067–3085. https://doi.
- org/10.1175/jcli-d-19-0959.1

 Wu, M., & Luo, Y. (2016). Mesoscale observational analysis of lifting mechanism of a warm-sector convective system producing the maximal daily precipitation in China mainland during pre-summer rainy season of 2015. *Journal of Meteorological Research*, 30(5), 719–736. https://
- doi.org/10.1007/s13351-016-6089-8
 Wu, N., Ding, X., Wen, Z., Chen, G., Meng, Z., Lin, L., & Min, J. (2020). Contrasting frontal and warm-sector heavy rainfalls over south China
- during the early-summer rainy season. *Atmospheric Research*, 235, 104693. https://doi.org/10.1016/j.atmosres.2019.104693

 Xu, J., Ma, Z., Yan, S., & Peng, J. (2022). Do ERA5 and ERA5-land precipitation estimates outperform satellite-based precipitation products? A comprehensive comparison between state-of-the-art model-based and satellite-based precipitation products over mainland China. *Journal of Hydrology*, 605, 127353. https://doi.org/10.1016/j.jhydrol.2021.127353
- Xu, W. (2020). Thunderstorm climatologies and their relationships to total and extreme precipitation in China. *Journal of Geophysical Research:* Atmospheres, 125(19), e2020JD033152. https://doi.org/10.1029/2020JD033152
- Xu, X., Xue, M., Wang, Y., & Huang, H. (2017). Mechanisms of secondary convection within a Mei-Yu frontal mesoscale convective system in eastern China. *Journal of Geophysical Research: Atmospheres*, 122(1), 47–64. https://doi.org/10.1002/2016JD026017
- Yamaji, M., Takahashi, H. G., Kubota, T., Oki, R., Hamada, A., & Takayabu, Y. N. (2020). 4-year climatology of global drop size distribution and its seasonal variability observed by spaceborne dual-frequency precipitation radar. *Journal of the Meteorological Society of Japan Service II*, 98(4), 755–773. https://doi.org/10.2151/jmsj.2020-038
- Yang, H., Du, Y., Chen, Z., & Fang, J. (2024). Could developing frontal rainfall influence warm-sector rainfall? *Geophysical Research Letters*, 51(15), e2024GL110430. https://doi.org/10.1029/2024GL110430
- Yu, S., Luo, Y., Wu, C., Zheng, D., Liu, X., & Xu, W. (2022). Convective and microphysical characteristics of extreme precipitation revealed by multisource observations over the pearl river Delta at monsoon Coast. Geophysical Research Letters, 49(2), 12. https://doi.org/10.1029/2021e1097043

ZUO ET AL. 22 of 23



Journal of Geophysical Research: Atmospheres

- 10.1029/2024JD043270
- Zhai, R., Huang, C., Yang, W., Tang, L., & Zhang, W. (2023). Applicability evaluation of ERA5 wind and wave reanalysis data in the South China Sea. *Journal of Oceanology and Limnology*, 41(2), 495–517. https://doi.org/10.1007/s00343-022-2047-8
- Zhang, A., Chen, Y., Li, W., & Chen, S. (2023). Event-based precipitation characteristics related to cloud-top temperature during pre-summer rainy season over south China. *International Journal of Climatology*, 43(5), 2271–2286. https://doi.org/10.1002/joc.7974
- Zhang, H., Zhou, Y., Lai, Z., & Deng, G. (2024). Overshooting convection and torrential precipitation associated with the mesoscale northerly low-level jets in the sichuan basin, China. *Atmospheric Research*, 310, 107604. https://doi.org/10.1016/j.atmosres.2024.107604
- Zhang, L. N., Short Gianotti, D. J., & Entekhabi, D. (2023). Land surface influence on convective available potential energy (CAPE) change during interstorms. *Journal of Hydrometeorology*, 24(8), 1365–1376. https://doi.org/10.1175/JHM-D-22-0191.1
- Zhao, S., Bei, N., & Sun, J. (2007). Mesoscale analysis of a heavy rainfall event over Hong Kong during a pre-rainy season in south China. *Advances in Atmospheric Sciences*, 24(4), 555–572. https://doi.org/10.1007/s00376-007-0555-2
- Zhong, S., & Yang, S. (2020). Nocturnal-to-morning rains during the warm season in south China: Characteristics and predictability. Atmospheric and Oceanic Science Letters, 13(6), 527–533. https://doi.org/10.1080/16742834.2020.1820844

References From the Supporting Information

- Cui, W., Dong, X., Xi, B., & Liu, M. (2020). Cloud and precipitation properties of MCSs along the meiyu frontal zone in central and southern China and their associated large-scale environments. *Journal of Geophysical Research: Atmospheres*, 125(6), e2019JD031601. https://doi.org/ 10.1029/2019JD031601
- Dougherty, E., Prein, A., Gutmann, E., & Newman, A. (2023). Future simulated changes in central US mesoscale convective system rainfall caused by changes in convective and stratiform structure. *Journal of Geophysical Research: Atmospheres*, 128(4), e2022JD037537. https://doi.org/10.1029/2022JD037537
- Fan, J., Wang, Y., Rosenfeld, D., & Liu, X. (2016). Review of aerosol-cloud interactions: Mechanisms, significance, and challenges. *Journal of the Atmospheric Sciences*, 73(11), 4221–4252. https://doi.org/10.1175/JAS-D-16-0037.1
- Fu, Y., Sun, J., Fu, S., & Zhang, Y. (2023). Comparison between warm-sector and frontal heavy rainfall events in south China and the objective classification of warm-sector heavy rainfall events. *Meteorology and Atmospheric Physics*, 135(1), 11. https://doi.org/10.1007/s00703-022-00940-8
- Li, S., Meng, Z., & Wu, N. (2021). A preliminary study on the organizational modes of mesoscale convective systems associated with warm-sector heavy rainfall in south China. *Journal of Geophysical Research: Atmospheres, 126*(16), 1. https://doi.org/10.1029/2021jd034587
- Prein, A. F., & Heymsfield, A. J. (2020). Increased melting level height impacts surface precipitation phase and intensity. *Nature Climate Change*, 10(8), 771–776. https://doi.org/10.1038/s41558-020-0825-x
- Thomas, A., Kanawade, V. P., Chakravarty, K., & Srivastava, A. K. (2021). Characterization of raindrop size distributions and its response to cloud microphysical properties. *Atmospheric Research*, 249, 105292. https://doi.org/10.1016/j.atmosres.2020.105292
- Wang, C., Chen, X., Zhao, K., & Peng, C. H. (2024). Synoptic control on the initiation and rainfall characteristics of warm-season MCSs over the south China Coast. *Journal of Geophysical Research: Atmospheres*, 129(8), e2023JD039232. https://doi.org/10.1029/2023JD039232
- Zhong, S., Li, X., Yang, S., & Chen, Z. T. (2019). Characteristics and synoptic environment of torrential rain in the warm sector over south China: A composite study. *Meteorology and Atmospheric Physics*, 131(5), 1191–1203. https://doi.org/10.1007/s00703-018-0629-y

ZUO ET AL. 23 of 23